

# Gaussian-LIC2: LiDAR-Inertial-Camera Gaussian Splatting SLAM

Xiaolei Lang<sup>1,†</sup>, Jiajun Lv<sup>1,†</sup>, Kai Tang<sup>1</sup>, Laijian Li<sup>1</sup>, Jianxin Huang<sup>1</sup>, Lina Liu<sup>1</sup>, Yong Liu<sup>1,\*</sup>, Xingxing Zuo<sup>2,\*</sup>

**Abstract**—This paper proposes an innovative LiDAR-Inertial-Camera SLAM system with 3D Gaussian Splatting, which is the first to jointly consider visual quality, geometric accuracy, and real-time performance. It robustly and accurately estimates poses while building a photo-realistic 3D Gaussian map in real time that enables high-quality novel view RGB and depth rendering. To effectively address under-reconstruction in regions not covered by the LiDAR, we employ a lightweight zero-shot depth model that synergistically combines RGB appearance cues with sparse LiDAR measurements to generate dense depth maps. The depth completion enables reliable Gaussian initialization in LiDAR-blind areas, significantly improving system applicability for sparse LiDAR sensors. To enhance geometric accuracy, we use sparse but precise LiDAR depths to supervise Gaussian map optimization and accelerate it with carefully designed CUDA-accelerated strategies. Furthermore, we explore how the incrementally reconstructed Gaussian map can improve the robustness of odometry. By tightly incorporating photometric constraints from the Gaussian map into the continuous-time factor graph optimization, we demonstrate improved pose estimation under LiDAR degradation scenarios. We also showcase downstream applications via extending our elaborate system, including video frame interpolation and fast 3D mesh extraction. To support rigorous evaluation, we construct a dedicated LiDAR-Inertial-Camera dataset featuring ground-truth poses, depth maps, and extrapolated trajectories for assessing out-of-sequence novel view synthesis. Extensive experiments on both public and self-collected datasets demonstrate the superiority and versatility of our system across LiDAR sensors with varying sampling densities. Both the dataset and code will be made publicly available on project page [https://xingxingzuo.github.io/gaussian\\_lic2](https://xingxingzuo.github.io/gaussian_lic2).

**Index Terms**—LiDAR-Inertial-Camera SLAM, multi-sensor fusion, photo-realistic dense mapping, 3D Gaussian Splatting.

## I. INTRODUCTION

**S**IMULTANEOUS localization and mapping (SLAM) serves as a fundamental technology that facilitates spatial perception in both mixed reality systems and robotic applications. Remarkably, recent advances in radiance field representations, particularly Neural Radiance Fields (NeRF) [1] and 3D Gaussian Splatting (3DGS) [2], have pioneered a new paradigm in SLAM, namely radiance-field-based SLAM [3]. Powered by differentiable photo-realistic rendering, radiance field-based SLAM systems aim to provide both accurate pose estimation and photo-realistic 3D maps in real time, equipping robots with richer 3D scene understanding. These systems can

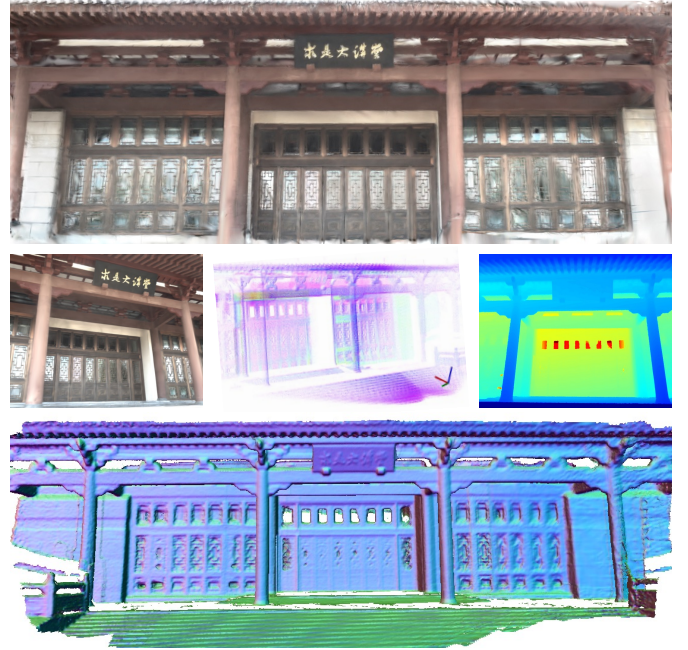


Figure 1: Overview of the system outputs (ordered left to right, top to bottom): (1) reconstructed map comprised of 3D Gaussians, (2) RGB image rendered from a novel viewpoint, (3) sparse LiDAR point cloud map, (4) depth map rendered from the novel viewpoint, and (5) 3D mesh extracted from the Gaussian map.

benefit a wide range of tasks, including path planning [4–6], active mapping [7, 8], and 3D mesh reconstruction [9].

Initially, NeRF-based SLAM systems [10–14] leverage multi-layer perceptrons (MLPs) to represent the entire scene and generate high-quality dense maps with low memory consumption. Nonetheless, such implicit representations necessitate computationally intensive volumetric rendering based on sampling in 3D space, undermining the real-time capability, which is essential for robot applications. The emergence of 3DGS has shifted this landscape. It features fast rendering along with superior visual quality and demonstrates greater potential for real-time use. Equipped with RGB-D or RGB sensors, most 3DGS-based SLAM systems [15–19] focus on indoor environments and outperform NeRF-based approaches, but unfortunately struggle in challenging conditions such as violent ego-motion, varying illumination, and lack of visual textures, commonly arising in unbounded outdoor scenes. Several works address the issue by fusing LiDAR and IMU [20–24], among which the effectiveness of LiDAR-Inertial-Camera fusion has been extensively validated in traditional SLAM methods [25–35]. Notably, the precise geometric priors provided by LiDAR contribute to both pose tracking and Gaussian

<sup>1</sup>Institute of Cyber-Systems and Control, Zhejiang University, China.

<sup>2</sup>Department of Robotics, Mohamed Bin Zayed University of Artificial Intelligence (MBZUAI).

<sup>†</sup>Contributed equally. \*Corresponding authors.

This work is supported by Zhejiang Provincial Natural Science Foundation of China under Grant No.LQN25F030006.

mapping, and the significantly reduced cost of LiDARs nowadays has made them much more accessible for integration.

Although existing LiDAR-Inertial-Camera 3DGS-based SLAM systems [20, 21, 23, 24, 36, 37] can achieve robust state estimation and dense mapping with high visual quality, several issues remain unresolved or insufficiently addressed. **First**, current methods predominantly rely on the dense LiDAR with the FoV closely aligned with that of the camera, initializing Gaussians solely from LiDAR points [22–24, 36]. This can lead to under-reconstruction in LiDAR blind spots, especially when the sparse LiDAR is used. Although adaptive density control (ADC) can alleviate this limitation by cloning and splitting Gaussians based on the magnitude of back-propagated gradients and scales of Gaussians [2], it struggles in the incremental SLAM systems involving optimization of Gaussians with different maturity. ADC also requires aggregating gradients over multiple iterations of optimization, which leads to a lack of timeliness for real-time SLAM systems. **Second**, despite leveraging LiDAR data with precise geometric information, existing SLAM methods overemphasize the visual quality of the map while neglecting its geometric reconstruction quality [21, 24, 36], which limits its applicability in geometry-critical tasks, like obstacle avoidance. Pursuing both high-quality RGB and depth rendering while maintaining real-time performance remains a great challenge. **Furthermore**, most existing methods [23, 24, 37] focus merely on rendering quality from training views, overlooking the novel view synthesis capability in sequence or even out of sequence. Admittedly, LiDAR-Inertial-Camera SLAM datasets that support RGB and depth rendering evaluation across both in-sequence and out-of-sequence novel views are scarce.

By combining 3D Gaussian Splatting with LiDAR-Inertial-Camera fusion, this paper addresses the aforementioned challenges and proposes a real-time photo-realistic SLAM system, dubbed Gaussian-LIC2. The system achieves robust and accurate pose estimation while constructing photo-realistic 3D Gaussian maps that encompass both high-fidelity visual and geometric information. Our main contributions are as follows:

- We propose the first LiDAR-Inertial-Camera Gaussian Splatting SLAM system that jointly takes care of visual quality, geometric accuracy, and real-time performance. It is capable of robustly and precisely estimating poses while constructing a photo-realistic and geometrically accurate 3D Gaussian map, all in real time.
- We propose integrating LiDAR and visual data through a fast, lightweight, generalizable sparse depth completion network to predict depths for pixels not covered by the LiDAR, enabling more comprehensive Gaussian initialization and mitigating under-reconstruction. During training, we fully leverage LiDAR-provided depth for supervision and accelerate the process with a series of meticulously designed C++ and CUDA implementations.
- We explore tightly fusing photometric constraints from the incrementally built Gaussian map with LiDAR-Inertial data in a continuous-time framework, successfully helping the odometry overcome the LiDAR degradation. Besides, we have extended our system to enable Gaussian map utilization for downstream applications such as video

frame interpolation and rapid mesh generation.

- We curate a specialized LiDAR-Inertial-Camera dataset that provides ground-truth poses and depth maps, along with carefully designed capturing trajectories, enabling the evaluation of out-of-sequence novel view synthesis. We conduct extensive experiments on public and self-collected datasets, demonstrating the superiority of our approach and its adaptability to various types of LiDARs.

## II. RELATED WORKS

### A. Photo-Realistic Reconstruction with Radiance Field

Map representation deeply affects architecture designs and potential downstream applications of SLAM systems. Sparse SLAM approaches [38, 39] excel in pose estimation but yield only sparse keypoint maps. On the contrary, dense SLAM methods produce dense maps beneficial for scene understanding. For instance, DTAM [40], REMODE [41], DSO [42], DROID-SLAM [43], etc. can achieve accurate camera pose tracking and reconstruct dense point cloud maps. KinectFusion [44], ElasticFusion [45], and SurfelMeshing [46] model 3D scenes using truncated signed distance function (TSDF), surfel, and mesh, all of which are commonly utilized in the SLAM field. However, it is challenging to recover photo-realistic camera views from these map representations. Fortunately, the emergence of NeRF [1] has brought a promising solution. As a novel radiance field representation, NeRF implicitly models the geometry and texture of the scene through MLPs and achieves differentiable photo-realistic rendering even at novel views. Plenoxels [47] and instant-ngp [48] further accelerate the training and inference of NeRF by introducing explicit feature grids. To improve the geometric accuracy of NeRF representation and extract a precise 3D mesh from it, VolSDF [49], NeuS [50], and NeuS2 [51] replace the density field with signed distance function (SDF).

However, NeRF still falls slightly short in real-time reconstruction due to the computationally intensive ray-based volume rendering. In contrast, 3D Gaussian Splatting (3DGS)[2] explicitly represents scenes using view-dependent anisotropic Gaussians and introduces a tile-based rasterization strategy for splats, achieving faster rendering speed while maintaining superior visual quality. Built upon 3DGS, a number of follow-up works have been proposed to further enhance its performance and flexibility. Scaffold-GS[52] incorporates tiny MLPs to predict the properties of neural Gaussians, enabling more compact and expressive representations. Meanwhile, SuGaR [53] and GOF [54] focus on efficient mesh extraction from 3DGS representations, facilitating downstream tasks such as geometry processing and simulation. 2DGS [55], GaussianSurfels [56], and PGSR [57] flatten the Gaussians to accurately conform to the scene surface, while RaDe-GS [58] introduces an enhanced depth rasterizing approach without the reformulation of the Gaussian primitives. NeuSG [59] and GSDF [60] try to combine neural SDF with 3DGS.

Original NeRF and 3DGS methods typically rely solely on image data for photo-realistic reconstruction. However, the incorporation of LiDAR, which has become increasingly affordable and accessible, can significantly enhance the performance of both NeRF and 3DGS, particularly in unbounded

outdoor environments. For NeRF, LiDAR data can guide ray sampling around surfaces and provide accurate depth supervision during optimization. URF[61] and EmerNeRF[62] are NeRF variants tailored for autonomous driving scenarios and achieve outstanding rendering quality with the aid of LiDAR. Bootstrapped by a LiDAR SLAM system, SiLVR[63] constructs multiple NeRF submaps efficiently. M2Mapping[64] further unifies surface reconstruction and photo-realistic rendering in LiDAR-Camera systems through an SDF-based NeRF formulation. In the context of 3DGS, LiDAR data can be leveraged not only for geometric supervision but also for the accurate and efficient initialization of 3D Gaussians. PVG [65], DrivingGaussian [66], StreetGaussians [67], and TCLC-GS [68] are the first to introduce LiDAR into the 3DGS framework, effectively modeling both static scenes and dynamic objects in autonomous driving environments. LIV-GaussMap [69] and LetsGo [70] both utilize the point cloud and poses from LiDAR-based SLAM to initialize 3DGS. Focusing more on geometric quality, LI-GS [71] employs 2DGS as the map representation to enhance surface alignment, while GS-SDF [72] incorporates LiDAR into SDF-based 3DGS.

The aforementioned works are all per-scene optimization frameworks. Interestingly, a series of feed-forward models [73–76] have emerged and achieved generalizable photo-realistic reconstruction in an end-to-end manner. However, their accuracy still lag behind that of per-scene optimization methods, and their applicability is limited to a small number of high-quality images with minimal viewpoint variation.

### B. Incremental Visual SLAM Systems with Radiance Field

Radiance-field-based reconstruction discussed in the last section, whether per-scene optimized or feed-forward, is essentially an offline process with all the collected data accessible. In comparison, radiance-field-based SLAM systems incrementally perform photo-realistic reconstruction with sequentially input sensor data, utilizing radiance file map representations.

Given sequential RGB-D inputs, iMAP [10] is a pioneering work built upon the implicit neural representation to achieve watertight online reconstruction. Following this, NICE-SLAM [11] is able to scale up to larger indoor scenes by combining MLP representation with hierarchical feature grids. Vox-Fusion [12] further adopts the octree to dynamically expand the volumetric map, eliminating the need for pre-allocated grids. Leveraging hash grids, tri-planes, and neural point cloud as their respective implicit representations, Co-SLAM [13], ESLAM [14], and Point-SLAM [77] get enhancement in both localization and mapping. Moreover, H2-Mapping [78] handles the forgetting issue by a novel coverage-maximizing keyframe selection strategy. In terms of 3DGS-based SLAM, GS-SLAM [15], SplatAM [16], and Gaussian-SLAM [17] demonstrate the advantages of 3DGS over existing map representations in SLAM systems for online photo-realistic mapping. By forcing binary opacity for each Gaussian, RTG-SLAM [79] achieves real-time performance indoors with the compact scene representation. GSFusion [80] jointly constructs the Gaussian map with a TSDF map and uses a quadtree data structure to reduce the number of Gaussians.

MM3DGS-SLAM [20] loosely fuses RGB-D and IMU measurements to enable more robust and precise pose estimation.

A range of studies have also explored operating solely on monocular RGB images, among which NICER-SLAM [81] and MonoGS [18] are the representative radiance-field-map-centric approaches. The former fully makes use of the monocular geometric cues for supervision, and the latter introduces the isotropic regularization to address ambiguities in incremental reconstruction. However, decoupled tracking and mapping methods, which adopt the state-of-the-art visual odometry for pose tracking and radiance field optimization for photo-realistic mapping in parallel, usually demonstrate much more robustness. Orbeez-SLAM [82] and Photo-SLAM [19] are both built upon the ORB-SLAM-based pose tracking [39]. NeRF-SLAM [83] and IG-SLAM [84] utilize the dense depth maps estimated from the tracking front-end DROID-SLAM as additional information to supervise the training of instantngp and 3DGS. NeRF-VO [85] and MGS-SLAM [86] instead employ the sparse DPVO [87] as a faster tracker with network-predicted dense depth maps for supervision.

### C. LiDAR-Integrated SLAM Systems with Radiance Field

Radiance-field-based Visual SLAM has achieved great performance in confined indoor scenes, and fusing IMU data can further improve the robustness. But they are still challenged by extreme violent motions, drastic lighting changes, and texture deficiency. Studies in both radiance-field-based reconstruction [61–72] and conventional SLAM [25–35] have validated the superiority of introducing LiDARs. For radiance-field-based SLAM, the advantages of integrating LiDAR include, at the very least, enhanced robustness and accuracy in pose estimation, precise geometric supervision, facilitating efficient sampling for NeRF and accurate initialization for 3DGS.

Powered by the LiDAR data, SHINE-Mapping [88] is an incremental mapping framework that uses octree-based hierarchical neural SDF to perform large-scale 3D reconstruction in a memory-efficient way. Meanwhile, NF-Atlas [89] organizes multiple neural submaps by a pose graph, and N3-Mapping [90] applies a voxel-oriented sliding window mechanism to alleviate the forgetting issue with a bounded memory footprint. Instead of purely geometric mapping, HGS-Mapping [91] incrementally builds a dense photo-realistic map with hybrid Gaussians in urban scenarios. All these mapping systems assume a priori ground-truth poses, whereas full SLAM systems that estimate poses simultaneously are inherently more complicated. NeRF-LOAM [92] is a typical NeRF-based LiDAR odometry and mapping method, optimizing poses and voxel embeddings concurrently. Furthermore, LONER [93] proposes a novel information-theoretic loss function to attain real-time performance. Benefiting from a semi-explicit representation, PIN-SLAM [94] utilizes a neural point cloud map representation with elasticity for globally consistent mapping. Splat-LOAM [95] exploits explicit 2DGS primitives with spherical projection for localization and LiDAR mapping.

Going beyond merely recovering the geometric structure of the scene, Rapid-Mapping [9] utilizes NeRF to represent and render detailed scene textures. MM-Gaussian [36], LiV-GS [22], and PINGS [96] perform coupled pose tracking and

dense mapping within a unified 3DGS optimization framework using LiDAR-Camera data. While these methods demonstrate impressive performance, they are not capable of real-time operation, despite the inherent efficiency of 3DGS. In contrast, decoupled tracking and Gaussian mapping approaches have shown promising results. Notably, Gaussian-LIC [21] is the first real-time LiDAR-Inertial-Camera 3DGS-based SLAM system, combining continuous-time LiDAR-Inertial-Camera odometry for tracking with 3DGS for mapping, achieving high-fidelity photo-realistic reconstruction in real time. Subsequently, GS-LIVM [37], LVI-GS [23], and GS-LIVO [24] have also been built atop classical LiDAR-Inertial-Camera odometry. Among them, GS-LIVM [37] and GS-LIVO [24] adopt voxel-based map structures and initialize Gaussian covariances. However, all these methods heavily rely on dense LiDAR sensors with the FoV aligned with that of the camera, and typically initialize Gaussians solely from LiDAR points. These approaches lead to under-reconstruction in LiDAR blind spots and suboptimal performance when using sparse LiDAR sensors. Notably, Gaussian-LIC incorporates online triangulation of visual features to compensate for regions not covered by the LiDAR. However, it struggles in textureless scenarios and is sensitive to parallax between views, which affects triangulation reliability. Furthermore, Gaussian-LIC primarily emphasizes visual rendering quality while overlooking geometric accuracy, such as dense depth rendering. The potential of leveraging the 3D Gaussian map to enhance pose tracking performance also remains underexplored in Gaussian-LIC.

In this paper, we propose a meticulous LiDAR-Inertial-Camera Gaussian Splatting SLAM system. In contrast to prior methods, our approach jointly considers visual fidelity, geometric precision, and real-time performance. It simultaneously estimates poses and constructs a photo-realistic Gaussian map in real time, enabling high-quality RGB and depth rendering.

### III. SYSTEM OVERVIEW

Fig. 2 depicts the overview of our proposed Gaussian-LIC2, which consists of two main modules: a continuous-time tightly-coupled LiDAR-Inertial-Camera Odometry and an incremental photo-realistic mapping back-end with 3DGS.

In the rest sections, we first present the formulation of continuous-time trajectory in Sec. IV and introduce the preliminaries of 3DGS in Sec. V. Next, in Sec. VI, we design a tightly-coupled LiDAR-Inertial-Camera odometry system as the front-end which supports two optional camera factors tightly fused within a continuous-time factor graph, including constraints from the Gaussian map. We then utilize an efficient but generalizable depth model to fully initialize Gaussians and prepare mapping data for the back-end in Sec. VII. Finally, we perform photo-realistic Gaussian mapping with depth regularization and CUDA-related acceleration in Sec. VIII.

### IV. CONTINUOUS-TIME TRAJECTORY FORMULATION

Two non-uniform cumulative B-splines, parameterizing the 3D rotation and the 3D translation, can jointly represent a

continuous-time trajectory. The 6-DoF poses at time  $t \in [t_i, t_{i+1})$  of a continuous-time trajectory are denoted by:

$$\mathbf{R}(t) = F_1(\mathbf{R}_{i-3}, \dots, \mathbf{R}_i, t_i, t_{i+1}, t), \quad (1)$$

$$\mathbf{p}(t) = F_2(\mathbf{p}_{i-3}, \dots, \mathbf{p}_i, t_i, t_{i+1}, t), \quad (2)$$

where  $\mathbf{R}_n \in SO(3)$  and  $\mathbf{p}_n \in \mathbb{R}^3$  denote control points ( $n \in \{i-3, \dots, i\}$ ).  $t_i$  and  $t_{i+1}$  represent two adjacent knots. The functions  $F_1$  and  $F_2$  derive poses from control points, knots, and querying time. Refer to [34, 35, 97] for more details.

The continuous-time trajectory of IMU in the world frame  $\{W\}$  is denoted as  ${}^W_I \mathbf{T}(t) = [{}^W_I \mathbf{R}(t), {}^W_I \mathbf{p}_I(t)]$ . Given known extrinsics between LiDAR/camera and IMU, we can handily get LiDAR trajectory  ${}^W_L \mathbf{T}(t)$  and camera trajectory  ${}^W_C \mathbf{T}(t)$ .

### V. 3D GAUSSIAN SPLATTING REPRESENTATION

Due to the strengths of 3DGS illustrated in Sec. II, we reconstruct a richly detailed photo-realistic map using a set of anisotropic 3D Gaussians. Each Gaussian is characterized by spatial position  $\boldsymbol{\mu} \in \mathbb{R}^3$ , scale  $\mathbf{S} \in \mathbb{R}^3$ , rotation  $\mathbf{R} \in \mathbb{R}^{3 \times 3}$ , opacity  $o \in \mathbb{R}$ , and three-degree spherical harmonics coefficients  $\mathbf{SH} \in \mathbb{R}^{3 \times 16}$  to encode view-dependent appearance of the scene [2]. Note that we do not compromise map quality for speed by employing isotropic and view-independent Gaussians as prior works [16, 20]. Instead, we retain the original expressive parameterization [2] and adopt the acceleration strategies described in Sec. X-D to pursue both quality and efficiency.

Representing the Gaussian's ellipsoidal shape, the covariance of each Gaussian is parameterized as  $\boldsymbol{\Sigma} = \mathbf{R}\mathbf{S}\mathbf{S}^T\mathbf{R}^T$ . Given a camera pose  ${}^C_W \mathbf{T} = \{{}^C_W \mathbf{R}, {}^C_W \mathbf{p}_W\}$ , which maps a 3D point  ${}^W \mathbf{p}$  from the world frame  $\{W\}$  to the camera frame  $\{C\}$ , a 3D Gaussian  $\mathcal{N}(\boldsymbol{\mu}, \boldsymbol{\Sigma})$  can be splatted onto the image screen, resulting in a corresponding 2D Gaussian  $\mathcal{N}(\boldsymbol{\mu}', \boldsymbol{\Sigma}')$ :

$$\boldsymbol{\mu}' = \pi_c \left( \frac{\hat{\boldsymbol{\mu}}}{\mathbf{e}_3^\top \hat{\boldsymbol{\mu}}} \right), \quad \hat{\boldsymbol{\mu}} = {}^C_W \mathbf{R} \boldsymbol{\mu} + {}^C_W \mathbf{p}_W, \quad (3)$$

$$\boldsymbol{\Sigma}' = \mathbf{J} {}^C_W \mathbf{R} \boldsymbol{\Sigma} {}^C_W \mathbf{R}^T \mathbf{J}^T, \quad (4)$$

where  $\mathbf{e}_i$  is a  $3 \times 1$  vector with its  $i$ -th element to be 1 and the other elements to be 0. Thus,  $\mathbf{e}_3^\top \hat{\boldsymbol{\mu}}$  gives the depth  $d$  of the 3D Gaussian in the camera frame. The function  $\pi_c(\cdot)$  projects a 3D point on the normalized image plane to a pixel.  $\mathbf{J} \in \mathbb{R}^{2 \times 3}$  represents the Jacobian of the affine approximation to the perspective projection [2]. The projected 2D Gaussian contributes to the image at pixel  $\boldsymbol{\rho} = [u \ v]^\top$  with a weight:

$$\alpha = o \exp \left( -\frac{1}{2} (\boldsymbol{\mu}' - \boldsymbol{\rho})^T (\boldsymbol{\Sigma}')^{-1} (\boldsymbol{\mu}' - \boldsymbol{\rho}) \right). \quad (5)$$

By arranging all the successfully splatted 3D Gaussians in depth order, the color, depth, and opacity at pixel  $\boldsymbol{\rho}$  can be efficiently rendered using front-to-back  $\alpha$ -blending:

$$\mathbf{C}(\boldsymbol{\rho}) = \sum_{i=1}^n \mathbf{c}_i \alpha_i \prod_{j=1}^{i-1} (1 - \alpha_j), \quad (6)$$

$$\mathbf{D}(\boldsymbol{\rho}) = \sum_{i=1}^n d_i \alpha_i \prod_{j=1}^{i-1} (1 - \alpha_j), \quad (7)$$

$$\mathbf{O}(\boldsymbol{\rho}) = \sum_{i=1}^n \alpha_i \prod_{j=1}^{i-1} (1 - \alpha_j), \quad (8)$$

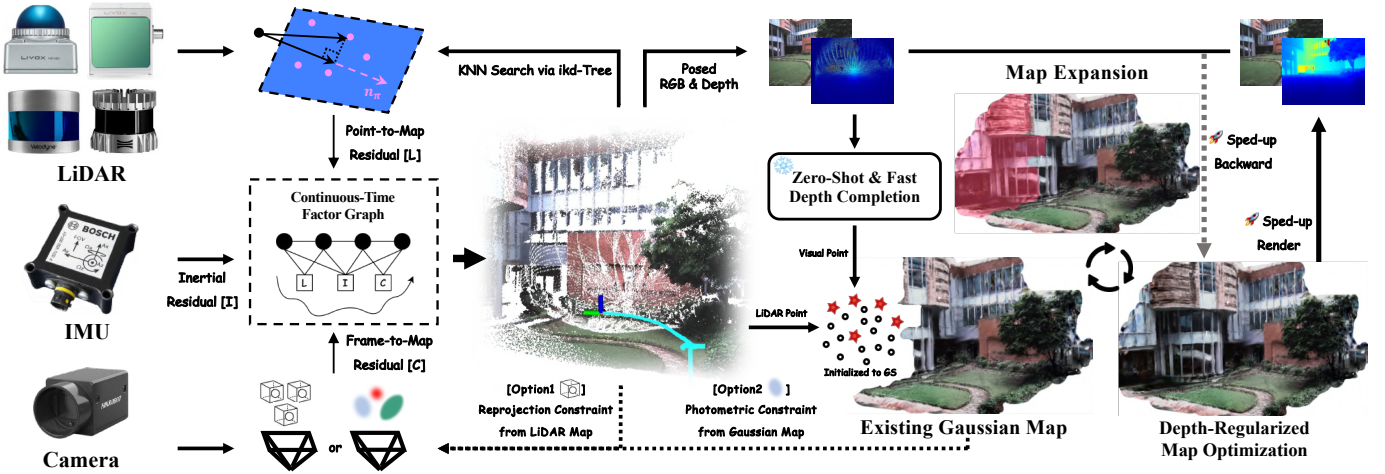


Figure 2: Pipeline of our real-time photo-realistic LiDAR-Inertial-Camera SLAM system, which represents the map using 3D Gaussians.

where  $\mathbf{c}$  denotes the view-dependent color of the 3D Gaussian derived from spherical harmonics  $\mathbf{SH}_b \in \mathbb{R}^{16}$  (as basis functions) and the corresponding coefficients  $\mathbf{SH}$  (as weights), while  $\mathbf{SH}_b$  is computed from the viewing direction between the Gaussian position  $\boldsymbol{\mu}$  and the camera position  ${}^c\mathbf{p}_W$  [2].

To investigate the constraint of the Gaussian map on pose estimation, we analytically compute the Jacobian of the 3DGS representation w.r.t camera pose on the manifold according to MonoGS [18], thereby avoiding the overhead of automatic differentiation. In contrast to MonoGS that models appearance with view-independent color, we further include the Jacobian of high-order spherical harmonics w.r.t the camera pose.

## VI. LiDAR-INERTIAL-CAMERA FUSION

We draw on the insights of classic multi-sensor fused odometry to achieve real-time, robust, and accurate pose estimation, paving the way for subsequent photo-realistic mapping. Specifically, our odometry system is inherited from and further developed based on Coco-LIC [35], a continuous-time tightly-coupled LiDAR-Inertial-Camera odometry using non-uniform B-spline. By leveraging the continuous-time trajectory representation, which inherently supports pose querying at any timestamp corresponding to sensor measurements, we seamlessly and tightly fuse asynchronous, high-frequency LiDAR-Inertial-Camera data without introducing interpolation errors. This results in improved stability and precision [34, 35].

### A. Trajectory Extension

Our LiDAR-Inertial-Camera system is initialized from a stationary state, using a buffer of IMU measurements to initialize IMU biases and the gravity-aligned orientation [98]. The system adopts an active sliding window of the latest 0.1 seconds for optimization, consistent with Coco-LIC [35].

Starting from time instant  $t_{\kappa-1}$ , we estimate the trajectory in  $[t_{\kappa-1}, t_{\kappa})$  once the LiDAR-Inertial-Camera data in the sliding window time interval is ready, where  $t_{\kappa} = t_{\kappa-1} + 0.1$ . The accumulated data contains all LiDAR raw points  $\mathcal{L}_{\kappa}$ , all IMU raw data  $\mathcal{I}_{\kappa}$ , and the latest image frame  $\mathcal{F}_{\kappa}$  in  $[t_{\kappa-1}, t_{\kappa})$ . For simplicity, we omit other image frames captured within this interval, which we found does not affect performance. As in

Coco-LIC, we first adaptively initialize a variable number of control points based on the motion intensity inferred from the IMU data, and then insert these control points into the sliding window to extend the trajectory. The following states are then optimized within the sliding window:

$$\begin{aligned} \mathcal{X}^{\kappa} &= \{\Phi(t_{\kappa-1}, t_{\kappa}), \mathbf{x}_{I_b}^{\kappa}\}, \\ \mathbf{x}_{I_b}^{\kappa} &= \{\mathbf{b}_g^{\kappa-1}, \mathbf{b}_a^{\kappa-1}, \mathbf{b}_g^{\kappa}, \mathbf{b}_a^{\kappa}\}, \end{aligned} \quad (9)$$

where  $\Phi(t_{\kappa-1}, t_{\kappa})$  denotes all control points within the interval  $[t_{\kappa-1}, t_{\kappa})$ , parameterizing the continuous-time trajectory of the IMU in the world frame.  $\mathbf{x}_{I_b}^{\kappa}$  denotes the IMU bias, which includes the gyroscope bias  $\mathbf{b}_g$  and the accelerometer bias  $\mathbf{b}_a$ . The IMU biases during  $[t_{\kappa-1}, t_{\kappa})$  are assumed to be constant as  $\mathbf{b}_g^{\kappa-1}$  and  $\mathbf{b}_a^{\kappa-1}$ . They are under Gaussian random walk and evolve to  $\mathbf{b}_g^{\kappa}$  and  $\mathbf{b}_a^{\kappa}$  at  $t_{\kappa}$ .

### B. Continuous-Time Factor Graph

1) *LiDAR Factor*: Different from Coco-LIC with LiDAR feature extraction and kd-Tree-organized map, we here directly register downsampled LiDAR raw points to the LiDAR map organized by the ikd-Tree for enhanced efficiency and accuracy [99]. Given a raw LiDAR point  ${}^L\mathbf{p} \in \mathcal{L}_k$  measured at time  $t$ , we first transform it to the world frame with the queried pose from the continuous-time trajectory, and then search for its five nearest neighbors in the LiDAR map to fit a 3D plane for a point-to-plane residual:

$$\mathbf{r}_L = {}^W\mathbf{n}_{\pi}^{\top} {}^W\hat{\mathbf{p}} + {}^Wd_{\pi}, \quad {}^W\hat{\mathbf{p}} = {}^W\mathbf{R}(t){}^L\mathbf{p} + {}^W\mathbf{p}_L(t), \quad (10)$$

where  ${}^W\mathbf{n}_{\pi}$  and  ${}^Wd_{\pi}$  denote the unit normal vector and the distance of the plane to the origin, respectively.

2) *Inertial Factor*: We define the following inertial factors:

$$\mathbf{r}_I = \begin{bmatrix} {}^I\boldsymbol{\omega}(t) - {}^I\boldsymbol{\omega}_m + \mathbf{b}_g^{\kappa-1} \\ {}^I\mathbf{a}(t) - {}^I\mathbf{a}_m + \mathbf{b}_a^{\kappa-1} \end{bmatrix}, \quad \mathbf{r}_{I_b} = \begin{bmatrix} \mathbf{b}_g^{\kappa} - \mathbf{b}_g^{\kappa-1} \\ \mathbf{b}_a^{\kappa} - \mathbf{b}_a^{\kappa-1} \end{bmatrix}, \quad (11)$$

where the former is the IMU factor and the latter is the bias factor based on the random walk process.  ${}^I\boldsymbol{\omega}_m, {}^I\mathbf{a}_m$  are the raw measurements of angular velocity and linear acceleration of the IMU data at time  $t$  in  $\mathcal{I}_{\kappa}$ .  ${}^I\boldsymbol{\omega}(t)$  and  ${}^I\mathbf{a}(t)$  are the corresponding predicted values computed from the derivatives of the continuous-time trajectory in Eq.(1) and Eq.(2) [35].

3) *Camera Factor (Option 1, Default)*: Our odometry system incorporates two types of camera factors, the first of which is based on reprojection constraints using the reconstructed LiDAR point map. Specifically, similar to Coco-LIC [35], we maintain a subset of global LiDAR points stored in voxels and associate them with image pixels by projection, KLT sparse optical flow [100], and RASAC-based outlier removal. Consider a global LiDAR point  ${}^W\mathbf{p}$  associated with the pixel  $\rho = [u \ v]^T$  in the image frame at the timestamp  $t$ . The reprojection error for this LiDAR point is defined as:

$$\mathbf{r}_{C_1} = \pi_c \left( \frac{C \hat{\mathbf{p}}}{\mathbf{e}_3^T C \hat{\mathbf{p}}} \right) - \begin{bmatrix} u \\ v \end{bmatrix}, \quad C \hat{\mathbf{p}} = {}^W\mathbf{T}^{-1}(t) {}^W\mathbf{p}. \quad (12)$$

4) *Camera Factor (Option 2)*: The second type of camera factor fully leverages the incrementally constructed Gaussian map. Thanks to the continuous-time trajectory formulation, we can obtain the camera pose  ${}^W_C\mathbf{T}$  at any time instant within the interval  $[t_{\kappa-1}, t_\kappa)$ . Given the timestamp  $t$  at which the raw RGB image  $\mathbf{C}$  (treated as ground truth) of frame  $\mathcal{F}_\kappa$  is captured, we render an RGB image  $\hat{\mathbf{C}}(\mathcal{G}, {}^W_C\mathbf{T}(t))$  from the Gaussian map  $\mathcal{G}$  using Eq. (6). The rendered image is expected to closely match the raw image, enabling optimization of the camera pose by minimizing the rendering loss:

$$\mathcal{L} = \frac{1}{2} \left\| \hat{\mathbf{C}} - \mathbf{C} \right\|_1 + \frac{1}{2} \mathcal{L}_{\text{D-SSIM}}(\hat{\mathbf{C}}, \mathbf{C}), \quad (13)$$

where  $\mathcal{L}_{\text{D-SSIM}}$  is a D-SSIM term [2]. Low-image-gradient or low-opacity pixels are penalized [18], which is omitted here for simplicity. Besides, in unbounded outdoor scenes with highly variable illumination and under conditions of fluctuating camera exposure, a standalone RGB L1 loss is susceptible to these noises, which may corrupt gradient directions, leading to erroneous camera pose optimization. To this end, we additionally introduce the D-SSIM loss to enhance the optimization robustness by accounting for structural similarity. We perform  $N_t$  iterations using the Adam optimizer, during which the Gaussian map  $\mathcal{G}$  is kept fixed while the camera pose is iteratively optimized. The resulting optimized camera pose from Eq. (13) is denoted as  ${}^W_C\tilde{\mathbf{T}} = \{{}^W_C\tilde{\mathbf{R}}, {}^W_C\tilde{\mathbf{p}}_C\}$ , and below is the derived photometric constraint from the Gaussian map:

$$\mathbf{r}_{C_2} = \text{Log} \left( {}^W_C\mathbf{T}(t) {}^W_C\tilde{\mathbf{T}}^{-1} \right). \quad (14)$$

### C. LiDAR-Inertial-Camera Factor Graph Optimization

We jointly fuse LiDAR-Inertial-Camera data in the factor graph and formulate the following nonlinear least-squares problem to efficiently optimize states  $\mathcal{X}^\kappa$ :

$$\arg \min_{\mathcal{X}^\kappa} \left\{ \sum \|\mathbf{r}_L\|_{\Sigma_L}^2 + \sum \|\mathbf{r}_I\|_{\Sigma_I}^2 + \sum \|\mathbf{r}_{I_b}\|_{\Sigma_{I_b}}^2 + \sum \|\mathbf{r}_{C_x}\|_{\Sigma_C}^2 + \sum \|\mathbf{r}_{\text{prior}}\|_{\Sigma_{\text{prior}}}^2 \right\}, \quad (15)$$

which is solved via the Levenberg-Marquardt algorithm in Ceres Solver [101] and accelerated through the analytical derivatives. The camera factor  $\mathbf{r}_{C_x}$  can be chosen as either  $\mathbf{r}_{C_1}$  or  $\mathbf{r}_{C_2}$ . The former is a reprojection constraint from the LiDAR map, which is somewhat handcrafted but very lightweight, while the latter is a photometric constraint from the Gaussian

map, which consumes modest GPU computing resources but is more direct and natural. A comparative evaluation of the two factors will be presented in Sec. X.  $\mathbf{r}_{\text{prior}}$  is the prior factor from marginalization [35].  $\Sigma_L, \Sigma_I, \Sigma_{I_b}, \Sigma_C, \Sigma_{\text{prior}}$  are the corresponding measurement covariances.

## VII. DATA PREPARATION FOR GAUSSIAN MAPPING

### A. Mapping Data Grouping

After finishing the optimization of the latest trajectory segment in  $[t_{\kappa-1}, t_\kappa)$ , we ultimately obtain the accurate camera pose for the latest image frame  $\mathcal{F}_\kappa$ . All LiDAR raw points within this time interval, namely  $\mathcal{L}_\kappa$ , can be easily transformed into the world frame based on the optimized continuous-time trajectory. The posed image, together with the transformed LiDAR points, is jointly regarded as a hybrid frame, and we treat every fifth hybrid frame as a keyframe for photo-realistic mapping. If the current hybrid frame is selected as a keyframe, we merge all LiDAR points from the latest five hybrid frames into a single point cloud. This point cloud is then projected onto the current image plane to generate a sparse depth map. Next, we downsample the point cloud by randomly retaining one out of every  $N_p$  points. The downsampled point cloud is also projected onto the current image plane for coloring. Colorized points will be used for initializing 3D Gaussians, which will be discussed in Sec. VIII-A2. At this stage, the keyframe is fully constructed, consisting of a posed image, a sparse depth map, and a set of colorized LiDAR points.

### B. Instant Depth Completion

LiDARs are able to provide precise geometric priors for Gaussian initialization. However, due to the mismatch in FoV between the LiDAR and the camera, relying solely on LiDAR points would lead to under-reconstruction in LiDAR blind areas or when using the sparse LiDAR. Although the adaptive density control (ADC) from vanilla 3DGS [2] offers a partial relief, its effectiveness is limited in SLAM. The incremental insertion of Gaussians leads to inconsistent convergence among different batches of Gaussians, which may misguide gradient-based operations like cloning and splitting. Moreover, the reliance on multi-iteration gradient accumulation hinders the real-time performance of the system. Gaussian-LIC [21] leverages online triangulated visual features to compensate for regions unobserved by LiDAR. However, it struggles in textureless areas and is sensitive to inter-frame viewpoint variations. Therefore, further investigation is warranted to explore how visual cues can be more effectively leveraged for efficient Gaussian initialization. The central challenge lies in obtaining accurate depth for image pixels.

**Why should it be depth completion?** With the advancement of computer vision research, numerous methods have emerged for recovering dense depth from images. First, monocular relative depth estimation [102, 103] has made significant progress in predicting depth from a single RGB image. However, it inherently suffers from scale ambiguity. While least-squares alignment with metric LiDAR depth can be applied, it often fails to recover accurate metric scale across all image pixels—particularly in regions with poor

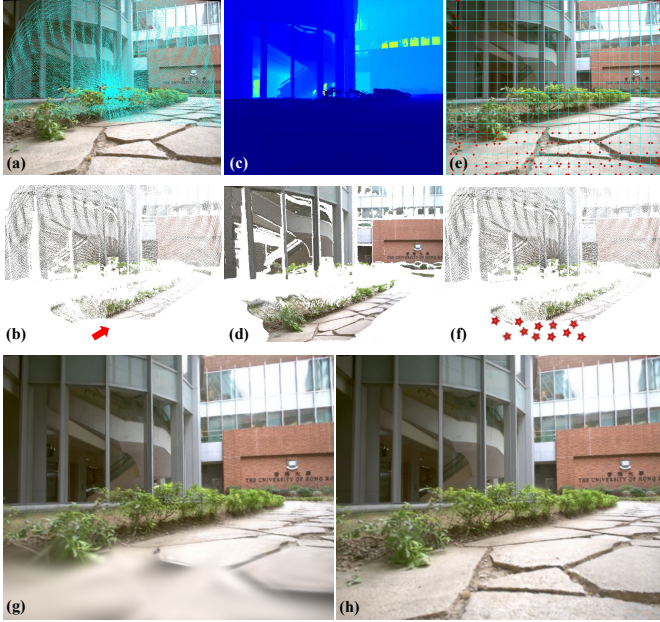


Figure 3: Details on the LiDAR depth completion: (a) Projection of LiDAR points of the latest 5 frames. (b) Colorized LiDAR points of the latest 5 frames. It is worth noting that the area highlighted by the red arrow has been never scanned by the LiDAR during the entire data acquisition. (c) Completed dense depth map. (d) Dense colored point cloud from the completed depth map. (e) The image is divided into  $30 \times 30$  patches, and the red dot denotes the selected pixels. (f) The red star indicates the 3D visual points obtained by back-projecting the selected pixels to compensate for the LiDAR blind area. (g) and (h) respectively show the rendering results of our method without and with depth completion.

relative depth estimation or lacking LiDAR coverage. Second, monocular metric depth estimation [104, 105] directly predicts scale-aware depth. However, its accuracy remains modest and lags far behind LiDAR-based methods, especially in large-scale outdoor environments. Third, multi-view stereo (MVS) approaches [106, 107] estimate metric depth from multiple posed images. Although MVS can produce accurate depth in favorable conditions, it is sensitive to parallax and exhibits limited generalization, particularly in large-scale outdoor scenes. In contrast, depth completion, which fuses sparse LiDAR data with a single RGB image, offers a practical and robust solution for recovering metric dense depth [108–110] in large-scale scenarios. It avoids the issue of scale ambiguity and can achieve LiDAR-comparable depth estimation accuracy.

In this paper, SPNet [110] is selected as the depth completer due to its efficiency, compactness, and strong generalization ability. We use it directly off the shelf, without any additional fine-tuning. As outlined in Alg. 1 and illustrated in Fig. 3, we feed the sparse depth map  $\mathbf{D}_s$  and the RGB image  $\mathbf{C}$  of the keyframe in Sec. VII-A into SPNet to generate a completed dense depth map  $\mathbf{D}_c$ . We then compute the mean depth change in the known regions before and after completion. If the depth change exceeds a threshold  $\epsilon_1$ , the completion is considered a failure (rarely occurring). After successful completion, pixels in  $\mathbf{D}_c$  with negative depth values or high depth gradient magnitudes are discarded, producing the filtered dense depth

---

**Algorithm 1: LiDAR Blind-Area Compensation**


---

**Input:** Sparse depth map  $\mathbf{D}_s$ , RGB image  $\mathbf{C}$   
**Output:** Supplemented colored point cloud  $\mathcal{P}$

- 1  $\mathcal{P} \leftarrow \emptyset, \mathcal{A} \leftarrow \emptyset$  // Initialize outputs
- 2  $\mathbf{M} \leftarrow \text{ValidMask}(\mathbf{D}_s)$
- 3  $\mathbf{D}_c \leftarrow \text{SPNet}(\mathbf{C}, \mathbf{D}_s, \mathbf{M})$
- 4  $\delta \leftarrow \text{Mean}(|(\mathbf{D}_c - \mathbf{D}_s)[\mathbf{M}]|)$
- 5 **if**  $\delta < \epsilon_1$  **then**
- 6      $\mathbf{D}_{c_f} \leftarrow \text{Filter}(\mathbf{D}_c)$
- 7     Divide  $\mathbf{D}_s$  into  $30 \times 30$  grid patches
- 8     **foreach** patch  $\mathcal{R}$  **in** grid **do**
- 9         **if**  $\text{IsEmpty}(\mathbf{D}_s[\mathcal{R}])$  **then**
- 10              $\rho \leftarrow \text{MinValidDepthPixel}(\mathbf{D}_{c_f}[\mathcal{R}])$
- 11             **if**  $\text{Depth}(\rho) < \epsilon_2$  **then**
- 12                  $\mathcal{A} \leftarrow \mathcal{A} \cup \{\rho\}$
- 13      $\mathcal{P} \leftarrow \text{BackProject}(\mathcal{A}, \mathcal{I})$
- 14 **return**  $\mathcal{P}$

---

map  $\mathbf{D}_{c_f}$ . Subsequently, we divide the input sparse LiDAR depth map into patches of size  $30 \times 30$  and iterate over each of them. For patches without any valid LiDAR depth, we select the pixel with the smallest completed depth within the patch of  $\mathbf{D}_{c_f}$  and store it in a container  $\mathcal{A}$  if its depth is less than  $\epsilon_2$ . All pixels in  $\mathcal{A}$  are back-projected to form a supplemented colored point cloud  $\mathcal{P}$ , compensating for LiDAR-unobserved regions. Finally,  $\mathcal{P}$  is transformed to the world frame and merged with the colored LiDAR points of the keyframe.

### VIII. REAL-TIME PHOTO-REALISTIC MAPPING

A mapping back-end thread runs in parallel with the tracking front-end thread and continuously receives sequential keyframes from the tracker to perform real-time photo-realistic reconstruction. Each keyframe contains an estimated camera pose, an undistorted image, a sparse LiDAR depth map, and a set of colored LiDAR points augmented with supplemented visual points derived from the completed dense depth map.

#### A. Gaussian Map Management

Once a keyframe is received, the mapping thread will initialize or expand the Gaussian map and optimize it.

1) *Initialization of Gaussian Map:* The Gaussian map is initialized using both the colored LiDAR points and the supplemented visual points from the first keyframe. Specifically, for each point, a new Gaussian is instantiated at its 3D location, with the zeroth degree of  $\mathbf{SH}$  initialized using its RGB color, opacity set to 0.1, and rotation initialized as the identity matrix. To mitigate aliasing artifacts as discussed in [111], we adapt the scale of each Gaussian based on its distance to the image plane [16, 21]. The scale is modeled as  $\mathbf{S} = \frac{d}{f} \mathbf{e}$ , where  $\mathbf{e}$  is a  $3 \times 1$  vector of ones,  $d$  is the depth of the 3D point in the camera frame, and  $f$  is the focal length.

2) *Expansion of Gaussian Map:* Each incoming keyframe typically captures new geometric and appearance information. However, the colored LiDAR points and supplemented visual points from consecutive keyframes often contain redundant 3D

points, resulting in excessive points for Gaussian initialization. To ensure high efficiency, we selectively initialize Gaussians using selected 3D points. Similar to previous works [16, 21], we first render an opacity map  $\mathbf{O}$  from the perspective of the current keyframe using Eq. (8). A binary mask  $\mathbf{M}_o = \mathbf{O} < \tau$  ( $\tau$  is a constant threshold) is then constructed to identify potentially newly observed image regions. Only the 3D points projected into these image regions are used to initialize new Gaussians, thereby expanding the Gaussian map.

3) *Depth-Regularized Map Optimization*: After the initialization or expansion, we randomly sample  $K$  keyframes out of all keyframes to optimize the Gaussian map, preventing catastrophic forgetting and ensuring global geometric consistency. The selected keyframes are shuffled and sequentially used to update the map by minimizing the rendering loss:

$$\mathcal{L} = \mathcal{L}_c + \xi \mathcal{L}_d, \quad (16)$$

$$\mathcal{L}_c = (1 - \lambda) \left\| \hat{\mathbf{C}} - \mathbf{C} \right\|_1 + \lambda \mathcal{L}_{\text{D-SSIM}}(\hat{\mathbf{C}}, \mathbf{C}), \quad (17)$$

$$\mathcal{L}_d = \left\| \left( \frac{\hat{\mathbf{D}}}{\hat{\mathbf{O}}} - \mathbf{D}_s \right) \cdot \mathbf{M}_d \right\|_1, \quad \mathbf{M}_d = \mathbf{D}_s > 0, \quad (18)$$

where  $\mathcal{L}_c$  denotes the RGB rendering loss computed by the rendered image  $\hat{\mathbf{C}}$  based on Eq.(6) and the raw image  $\mathbf{C}$ , while  $\mathcal{L}_d$  is the depth rendering loss involved with the rendered depth map  $\hat{\mathbf{D}}$  via Eq.(7) and the sparse LiDAR depth map  $\mathbf{D}_s$ . Note that we utilize the rendered opacity map  $\hat{\mathbf{O}}$  to normalize the rendered depth map in incremental mapping.

### B. CUDA-Related Acceleration Strategies

To improve real-time performance, previous works either forcibly limit the number of Gaussians or simplify the Gaussian representation [16, 79], which might work well indoor but often degrades performance in unbounded and complex outdoor scenarios. On the contrary, similar to [21], we concentrate on speeding up the CUDA-based operations, particularly the forward and backward of the 3DGS rasterizer, so as to ensure real-time performance without compromising the quality.

1) *Fast Tile-based Culling*: During the forward pass, 3D Gaussians are splatted onto the image, resulting in elliptical 2D Gaussians. To determine the tiles affected by each Gaussian, the elliptical 2D Gaussian is further dilated into a circle whose radius equals the major axis length [2]. However, such an approximation results in overly inflated tiles influenced by the Gaussian, particularly for highly anisotropic Gaussians, which are common in incremental mapping systems such as SLAM. To address this issue, we adopt a fast tile-based culling strategy, as illustrated in Fig. 4(a). For each 2D Gaussian  $\mathcal{N}(\boldsymbol{\mu}', \boldsymbol{\Sigma}')$  and the tiles affected by it, we identify the pixel  $\rho$  within every tile where the 2D Gaussian yields the highest contribution (with the max weight  $\alpha$  in Eq.(5)), as in [112]. If the weight  $\alpha$  at the pixel  $\rho$  is smaller than the threshold  $\frac{1}{255}$ , we regard the tile as weakly affected and cull it. In this way, the number of Gaussians per tile can be significantly reduced, accelerating the subsequent forward and backward pass.

2) *Per-Gaussian Backpropagation*: During the backward pass, gradients flow from RGB pixels back to Gaussians,

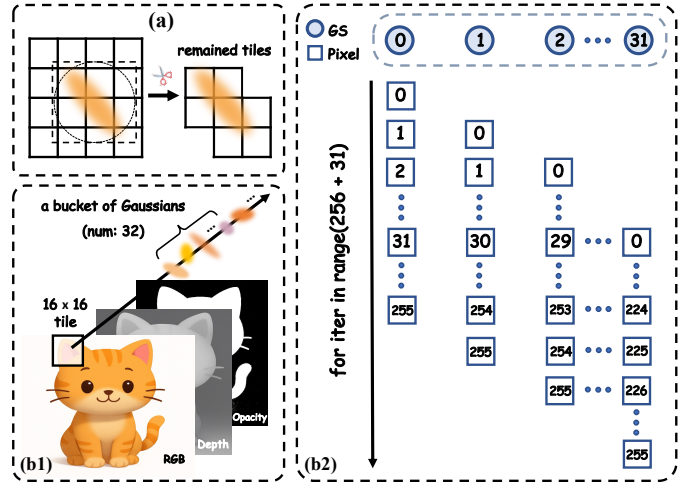


Figure 4: Acceleration strategies in the forward and backward pass when optimizing the Gaussian map: (a) Culling the tiles weakly affected by the splatted Gaussians. (b1) Every 32 Gaussians within a tile ( $16 \times 16$  pixels) are grouped into a bucket. (b2) All buckets are processed in parallel for  $(256+31)$  iterations (row by row). In each iteration, all Gaussians within the bucket accumulate gradients from different pixels for optimization with respect to the rendered RGB, depth, and opacity maps—without incurring atomic collisions.

which is the most time-consuming stage during the mapping [2]. Each pixel typically receives contributions from a different number of Gaussians, and the runtime is ultimately dominated by the pixel associated with the largest number of Gaussians. As a result, the remaining CUDA threads must wait idly, leading to significant inefficiency. Also, atomic gradient addition conflicts arise when multiple pixels backpropagate to the same Gaussian. To address these issues, we shift from pixel-wise parallelism to Gaussian-wise parallelism following [113], as illustrated in Fig. 4(b1) and (b2). To be specific, we divide the depth-sorted Gaussians within each tile into buckets of 32 Gaussians each. Then, all Gaussians across all buckets are processed in parallel. For a given bucket, all 32 Gaussians simultaneously iterate over pixels within the tile to accumulate gradients. As a result, the upper bound of the backward time is largely determined by the number of pixels, leading to more consistent computational load and reduced collisions. In this way, compared to [21, 113], in addition to the RGB channels, we also incorporate per-Gaussian gradient backpropagation for the depth map and the opacity map.

3) *Additional Strategies*: a) *Sparse Adam*. The original 3DGS [2] uses the Adam optimizer to update all Gaussians, including those not involved in the current rendering, by applying zero gradients. The computational burden becomes progressively unsustainable as the map size increases. Therefore, we adopt sparse Adam [113] to update only the valid Gaussians that participate in the rendering. b) *Separated SH*. In the original 3DGS framework, the low-order and high-order SH coefficients are concatenated before the forward and backward passes per iteration. However, the concatenation operation is time-consuming, especially when using three-degree SH in our method. To address this, we handle the low-order and high-order coefficients separately, eliminating

the concatenation. *c) Efficient SSIM.* We employ the highly efficient and differentiable SSIM implemented in [113], where separable Gaussian convolutions lead to reduced computation. *d) Warp-Level Predicate Masking.* The warp serves as a bridge between threads and blocks, which is crucial for parallel performance in GPU. Threads are typically operated in groups of 32 as a warp, and performance can degrade if threads within a warp diverge due to conditional branches. For example, in the forward pass of 3DGS, Gaussians handled by different threads may be deemed invalid—due to invalid depth, non-invertible 2D covariance, or insufficient weights—causing threads to exit under varying conditions, leading to divergence. To tackle this problem, we use flags to unify the return decisions in the final stage, avoiding divergence. Besides, we implement early stopping for warps in which all threads are flagged to return, improving efficiency. *e) CPU to GPU.* When optimizing the map, ground-truth images and sparse LiDAR depth maps need to be transferred from the CPU to the GPU, which incurs a certain amount of overhead. However, preloading them onto the GPU is not allowed due to limited memory. Thus, we store them in pinned memory and utilize non-blocking transfer to move data from the CPU to the GPU. This allows the transfer to be executed in parallel with GPU computation, improving computing asynchrony and overall throughput.

## IX. DATASETS FOR EVALUATION

This section describes the datasets used for evaluation, encompassing both public and self-collected ones. The public datasets, including R3LIVE [30], FAST-LIVO [32, 33], MCD [114], and M2DGR [115], are mainly employed for localization and in-sequence novel view rendering evaluation. Our self-collected dataset supports both in-sequence and out-of-sequence novel view rendering evaluation, and enables quantitative evaluation of rendered depth. Tab. VI summarizes the duration and length of each sequence.

### A. Public Dataset

The R3LIVE dataset [30] and FAST-LIVO dataset [32, 33] are both collected within the campuses using a handheld device equipped with a Livox Avia LiDAR at 10 Hz and its built-in IMU at 200 Hz, and a 15 Hz RGB camera. Closely aligned with the camera’s FoV and performing non-repetitive scanning, the projected points of the adopted solid-state LiDAR are distributed across the image, while still suffering from non-negligible blind spots as shown in Fig. 3. Six outdoor sequences from the R3LIVE dataset that are well-suited for mapping are selected for evaluation. The FAST-LIVO dataset used in this work includes all sequences from FAST-LIVO and the first two sequences from FAST-LIVO2, whose high-quality images make the dataset particularly suitable for mapping tasks. Notably, the R3LIVE and FAST-LIVO datasets also provide challenging sequences with LiDAR or visual degeneration, such as *degenerate\_seq\_00-01*, *LiDAR\_Degenerate*, and *Visual\_Challenge*. Although the ground-truth trajectory is unavailable, the start and end poses coincide, allowing localization evaluation via start-to-end drift. When stereo pairs are available, only the left image ( $640 \times 512$ ) is used.



Figure 5: Two types of LIC sensor rig for self-collected dataset.

The MCD dataset [114] provides sequences across seasons and continents, captured in large-scale campuses. We here pick the sequences (*tuhh\_day\_02-04*) with the repetitive mechanical spinning Ouster OS1-64 LiDAR at 10Hz, a 30 Hz RGB camera ( $640 \times 480$ ) and a 400 Hz IMU. The sparsity of spinning LiDAR poses greater challenges for LiDAR-based Gaussian mapping. Due to the extensive scale of the environment, we truncate the sequences to the first 200 seconds ( $\sim 300$  m). The dataset provides highly accurate ground-truth trajectories for quantitative evaluation of localization.

The M2DGR dataset [115], collected by a ground robot during both day and night using a Velodyne VLP-32C LiDAR at 10 Hz, an IMU at 100 Hz, and a 10 Hz RGB camera ( $640 \times 480$ ), presents a more challenging case due to the extremely sparse LiDAR measurements. A set of sequences (*room\_01-03*) under favorable lighting are selected for evaluation.

### B. Self-Collected Dataset

To further evaluate out-of-sequence novel view synthesis and quantitatively assess the accuracy of the rendered depth, we collect additional sequences leveraging two handheld devices in Fig. 5, enriching LiDAR modality diversity. The first setup integrates a Livox Mid-360 LiDAR sampled at 10 Hz paired with a 30 Hz RealSense D455 RGB camera ( $640 \times 480$ ). Compared to Avia, Mid-360 offers a wider horizontal FoV but shorter maximum ranging distance, presenting unique reconstruction challenges. Meanwhile, the second one follows the LIV\_handheld<sup>1</sup> configuration, combining a Livox Avia LiDAR at 10 Hz with a Hikvision MV-CA013-21UC RGB camera at 15 Hz ( $640 \times 512$ ). Both handheld systems utilize the built-in 200 Hz IMU from the LiDAR, with the LiDAR and the IMU factory-synchronized and well-calibrated. The spatial and temporal extrinsics between the camera and the IMU are carefully calibrated through Kalibr [116].

For each sequence, we capture a long and smooth trajectory with loop closures, ensuring the scene is revisited for out-of-sequence evaluation and making the captured data well-suited for mapping purposes. Due to unreliable GPS between buildings, GPS-based pose estimation is often unreliable. We generate continuous-time ground-truth trajectories using a LiDAR-Inertial-Camera SLAM framework that incorporates

<sup>1</sup>[https://github.com/xuankuzcr/LIV\\_handhold](https://github.com/xuankuzcr/LIV_handhold)

continuous-time loop closure [117] to enhance accuracy. Note that our captured scenes are not excessively large (i.e., not at an urban scale), and the estimated ground-truth trajectories are sufficiently accurate for evaluation purposes. For generating ground-truth depth maps, we query the camera pose from the ground-truth trajectory and project the temporally closest LiDAR frame onto the image. Each collected trajectory is divided into two segments, used respectively for in-sequence and out-of-sequence evaluations, as illustrated in Fig. 9.

## X. EXPERIMENT RESULTS

### A. Implementation Details

We implement the proposed system fully in C++ and CUDA. The tracking and mapping modules run in parallel and communicate via ROS, with the mapping built upon the LibTorch framework. The depth completion network SPNet [110] is deployed with TensorRT for efficient inference.

For odometry, we reuse the ikd-Tree parameters from FAST-LIO2 [99], set the camera pose optimization step  $N_t$  in Sec. VI-B4 to 30. For mapping data preparation, we set  $N_p$  in Sec. VII-A to 10 (Avia, Mid-360), 5 (OS1-64), and 1 (VLP-32C).  $\epsilon_1$  and  $\epsilon_2$  in Sec. VII-B are set to 0.1 m and 50 m, respectively. For map expansion, we set  $\tau$  in Sec. VIII-A2 to 0.99. As for map optimization, we set the loss weighting  $\lambda$  to 0.2 and  $\xi$  to 0.005, and the number  $K$  of selected keyframes to 100. All the learning rates for Gaussian attributes follow vanilla [2] but do not decay with schedulers. We keep the same hyperparameters in all sequences with the same sensor setup to ensure a fair and comprehensive evaluation. Experiments are run on a desktop PC with an NVIDIA RTX 4090 GPU (24 GB VRAM), Intel i9-13900KF CPU, and 64 GB RAM.

### B. Baselines

This paper focuses on developing an elaborated radiance-field-based SLAM system capable of robust and accurate pose estimation while constructing fine-grained photo-realistic 3D maps in real time. Therefore, our comparative analysis specifically targets authentic SLAM systems, explicitly excluding pure mapping systems that require a priori ground-truth poses.

We first evaluate localization performance against state-of-the-art traditional LiDAR-Inertial-Camera SLAM systems, including optimization-based LVI-SAM [28] and filter-based R3LIVE [30] and FAST-LIVO2 [33]. We also include two neural SLAM methods: PIN-SLAM [94], a neural LiDAR SLAM approach utilizing point-based NeRF for geometry-only reconstruction, and DBA-Fusion [118], which integrates IMU data into DROID-SLAM [43], currently the most advanced neural visual SLAM framework. We run PIN-SLAM by feeding in undistorted LiDAR point clouds.

Furthermore, to evaluate both the localization and photo-realistic mapping performances of the entire system, we compare against photo-realistic radiance-field-based SLAM, including both NeRF-based and 3DGS-based. 1) **NeRF-based:** As no related LiDAR-Camera system is publicly available, we adapt the state-of-the-art RGB-D NeRF-based method Co-SLAM [13] with pseudo RGB-D input by merging LiDAR scans. When rendering the full image, we use SPNet [110] to

complete the LiDAR depth maps for depth-guided sampling. 2) **3DGS-based:** We compare with the state-of-the-art RGB-only method MonoGS [18], which elegantly derives pose gradients. Given the scarcity of available LiDAR-Camera 3DGS-based methods, we run the state-of-the-art RGB-D 3DGS-based approach SplaTAM [16] using pseudo RGB-D images. We also compare against the RGB-D inertial method, MM3DGS-SLAM [20], which extends SplaTAM by incorporating IMU data, and include a comparison with the LiDAR-Inertial-Camera Gaussian Splatting SLAM framework Gaussian-LIC [21], where the sky modeling is disabled to facilitate depth rendering. For fair comparison, all methods are evaluated without loop closure and post-processing.

### C. Experiment-1: Evaluation of Localization

We validate the robustness and accuracy of our method tracking in both challenging degenerate and large-scale environments. In particular, we compare two types of camera factors presented in Sec. VI-B: option 1 (LiDAR map reprojection constraint, *Ours-1*) and option 2 (Gaussian map photometric constraint, *Ours-2*). Also, we investigate the effectiveness of the camera factor option 2 when the depth supervision (Eq. (18)) is disabled, denoted as *Ours-2-w/o-d*.

1) *Challenging Degenerate Sequences:* Sequences *degenerate\_seq\_00-01*, *LiDAR\_Degenerate*, and *Visual\_Challenge*, provided in the R3LIVE and FAST-LIVO datasets, exhibit severe degradation, such as the solid-state LiDAR with small FoV facing the ground or walls, and the camera facing textureless surfaces or undergoing aggressive motions (*Visual\_Challenge*). Tab. I reports the start-to-end drift (and rotation) errors. Methods that rely solely on the rendering loss from radiance field maps for localization, including MonoGS, Co-SLAM, SplaTAM, and MM3DGS-SLAM, achieve excellent localization accuracy in confined indoor scenarios with moderate view changes. However, they tend to fail in large-scale outdoor scenes with significant viewpoint variation, as the camera can easily enter regions where the map optimization has not yet converged. MonoGS is the only one that lacks an absolute scale, we align its estimated trajectory with that of *Ours-1* for obtaining the absolute scale. MM3DGS-SLAM, aided by IMU, completes the sequence *degenerate\_seq\_00*, but still fails on the rest. Based on a point-based NeRF presentation, PIN-SLAM optimizes the poses via point-to-model SDF loss [94], which is similar to the point-to-plane metric in ICP. It builds a purely geometric map and achieves robust pose optimization even in challenging lighting conditions, but suffers in LiDAR degradation scenarios where environmental structures fail to provide sufficient constraints for pose optimization. Moreover, relying solely on the LiDAR data and constant velocity assumption for initial pose, PIN-SLAM crashes on the sequence *Visual\_Challenge* where aggressive motions happen. As a learning-based visual-inertial odometry system, DBA-Fusion exhibits greater robustness to LiDAR degradation, and its tight fusion with IMU data facilitates handling of aggressive motions. Nevertheless, excessive view changes in the sequence *Visual\_Challenge* adversely affect the accuracy of the predicted dense optical flow thus significantly deteriorates the pose tracking in DBA-Fusion.

Table I: Localization Evaluation: The start-to-end drift error (translation | rotation) on challenging sequences. The best are in bold and the second best are underscored. × means failure. Note that, except for the sequence *LiDAR\_Degenerate*, which is an indoor sequence, all the others are outdoor sequences. Hybrid means using both the point cloud map and the 3DGS map for localization.

Method	Sensor	Map Type (for Loc)	Sequence							
			degenerate_seq_00		degenerate_seq_01		LiDAR_Degenerate		Visual_Challenge	
MonoGS [18]	C	3DGS	14.54m	67.40°	×	×	×	×	×	×
Co-SLAM [13]	L + C	NeRF	12.37m	30.50°	×	×	×	×	×	×
SplaTAM [16]	L + C	3DGS	17.96m	16.75°	×	×	×	×	×	×
MM3DGS-SLAM [20]	L + I + C	3DGS	9.14m	14.02°	×	×	×	×	×	×
PIN-SLAM [94]	L	NeRF	9.07m	30.05°	13.53m	29.29°	4.13m	3.71°	×	×
DBA-Fusion [118]	I + C	PointCloud	0.53m	8.98°	1.87m	1.93°	0.46m	4.66°	3.19m	6.21°
LVI-SAM [28]	L + I + C	PointCloud	0.08m	6.60°	0.11m	2.67°	×	×	×	×
R3LIVE [30]	L + I + C	PointCloud	<u>0.04m</u>	<b>0.41°</b>	0.11m	<b>0.55°</b>	8.52m	2.99°	0.21m	0.69°
FAST-LIVO2 [33]	L + I + C	PointCloud	5.07m	8.38°	2.41m	6.20°	<b>0.02m</b>	<b>2.40°</b>	<b>0.02m</b>	<u>0.14°</u>
Gaussian-LIC [21]	L + I + C	PointCloud	<u>0.04m</u>	0.54°	0.06m	0.62°	<u>0.05m</u>	2.63°	0.07m	<u>0.30°</u>
Ours-1	L + I + C	PointCloud	<u>0.04m</u>	0.58°	<b>0.04m</b>	<b>0.55°</b>	<u>0.05m</u>	2.58°	<u>0.06m</u>	0.23°
Ours-2	L + I + C	Hybrid	<b>0.03m</b>	<u>0.43°</u>	<u>0.05m</u>	<u>0.59°</u>	<u>0.05m</u>	<u>2.50°</u>	<b>0.02m</b>	<b>0.11°</b>
Ours-2-w/o-d	L + I + C	Hybrid	7.12m	6.22°	0.45m	0.80°	3.27m	5.92°	0.10m	0.89°

Table II: Localization Evaluation: The RMSE (m) of APE results on large-scale outdoor sequences in MCD dataset [114].

	tuhh_day_02	tuhh_day_03	tuhh_day_04
MonoGS [18]	29.53	42.54	25.4
Co-SLAM [13]	47.26	×	×
SplaTAM [16]	×	34.49	×
MM3DGS-SLAM [20]	17.53	20.14	26.33
PIN-SLAM [94]	0.16	0.11	0.38
DBA-Fusion [118]	1.86	1.25	2.71
LVI-SAM [28]	0.14	0.13	0.18
R3LIVE [30]	0.10	0.13	0.15
FAST-LIVO2 [33]	<b>0.08</b>	0.11	0.13
Gaussian-LIC [35]	<b>0.08</b>	0.09	0.10
Ours-1	<b>0.08</b>	<b>0.08</b>	<b>0.09</b>
Ours-2	<b>0.08</b>	0.09	<b>0.09</b>

Among all the comparisons, LiDAR-Inertial-Camera fusion-based methods with each module meticulously designed showcase more robust and accurate performance. Rather than separately fusing LiDAR-inertial and visual-inertial data like LVI-SAM, R3LIVE, and FAST-LIVO2, our method maintains a single unified system that jointly and tightly integrates LiDAR-Inertial-Camera data within a continuous-time factor graph, achieving superior overall performance. Fig. 6 shows the trajectory and colored LiDAR map produced by *Ours-2*, where the odometry successfully overcomes severe LiDAR degradation challenges and returns to the origin with minor drift. A set of subfigures in Fig. 6 presents rendered images from three different viewpoints corresponding to poses predicted by the IMU, refined by Gaussian-map-based optimization ( ${}^W_C \tilde{T}$  in Eq. (14)), and further refined through LiDAR-Inertial-Camera factor graph optimization (Sec. VI-C). The increasing similarity between the rendered and raw images visually demonstrates the progressive refinement of the estimated pose. Interestingly, *Ours-2* outperforms *Ours-1* on the *Visual\_Challenge* sequence, which features textureless white walls. This improvement can be attributed to the photometric constraints derived from the Gaussian map, which enhance *Ours-2*'s robustness in low-texture environments compared to the optical-flow-based *Ours-1*. Without depth supervision, *Ours-2-w/o-d* shows reduced accuracy. The depth regularization prevents the Gaussian map from overfitting to training

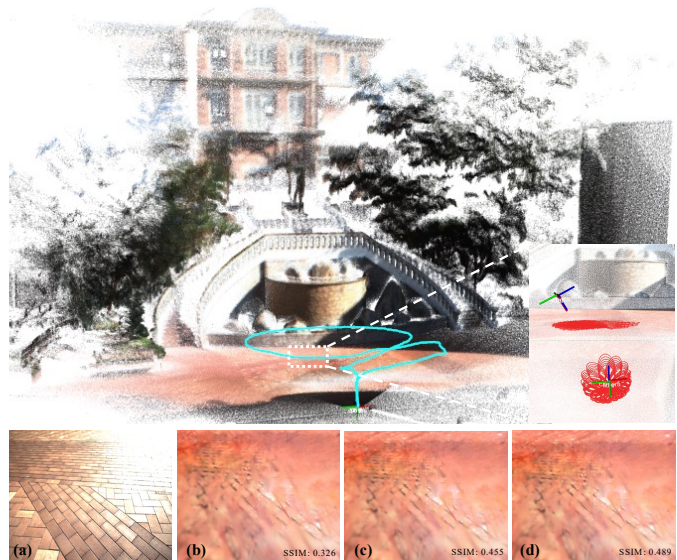


Figure 6: The trajectory and colored LiDAR point cloud map output by the continuous-time odometry tightly fused with the Gaussian map. Even undergoing severe degradation when the solid-state LiDAR faces the plain ground, the odometry performs pose estimation accurately with minor start-to-end drift error, benefiting from the photometric constraints provided by the Gaussian map. (a)-(d) are the raw image of the current view and rendered images from poses predicted by the IMU, refined by Gaussian-map-based optimization, and further optimized through LiDAR-Inertial-Camera factor optimization, respectively. Color discrepancies between the ground-truth and rendered images reflect variable illumination and varying camera exposure, highlighting the importance of the D-SSIM loss in Eq.(13).

views, which enables more robust novel view synthesis with fewer artifacts, as discussed in Sec. X-D. This is critical since localization based on Gaussian maps inherently requires continuous novel view synthesis from varying perspectives.

2) *Large-Scale Outdoor Sequences*: Tab. II displays the localization error across different methods in the large-scale scenes without sensor degradation. Rendering-based methods including MonoGS, Co-SLAM, SplaTAM, and MM3DGS-SLAM, exhibit reduced accuracy in pose estimation. Although MM3DGS-SLAM benefits from IMU-based pose initialization, its loosely coupled integration without accounting for

Table III: Evaluation of RGB rendering (in-sequence novel view) on public datasets.

Sequence	Rendering Performance (PSNR $\uparrow$ SSIM $\uparrow$ LPIPS $\downarrow$ )														
	MonoGS [18]			Co-SLAM [13]			MM3DGS-SLAM [20]			Gaussian-LIC [21]			Ours		
<b>R3LIVE (Avia)</b>															
degenerate_seq_00	14.59	0.460	0.624	14.42	0.286	0.810	19.35	0.698	0.212	21.94	0.777	0.171	<b>21.99</b>	<b>0.782</b>	<b>0.162</b>
degenerate_seq_01	14.66	0.438	0.692	14.88	0.267	0.822	18.57	0.621	0.277	22.80	0.787	0.169	<b>22.94</b>	<b>0.790</b>	<b>0.159</b>
hku_campus_00	15.41	0.464	0.675	15.50	0.302	0.794	18.70	0.621	0.319	<b>24.38</b>	<b>0.787</b>	0.162	24.34	<b>0.787</b>	<b>0.156</b>
hku_campus_01	8.39	0.065	0.873	12.92	0.294	0.796	16.97	0.593	0.271	<b>20.55</b>	0.671	0.275	20.52	<b>0.674</b>	<b>0.236</b>
hku_park_00	13.24	0.319	0.733	14.02	0.218	0.790	14.98	0.363	0.396	17.09	0.466	0.354	<b>17.17</b>	<b>0.469</b>	<b>0.340</b>
hku_park_01	12.22	0.289	0.790	13.65	0.207	0.815	15.79	0.392	0.409	19.45	<b>0.529</b>	0.340	<b>19.46</b>	<b>0.529</b>	<b>0.325</b>
<b>FAST-LIVO (Avia)</b>															
LiDAR_Degenerate	25.44	0.779	0.645	23.59	0.622	0.496	28.58	0.828	0.157	30.09	0.829	0.155	<b>30.36</b>	<b>0.831</b>	<b>0.144</b>
Visual_Challenge	15.36	0.563	0.674	15.96	0.365	0.711	17.62	0.712	0.240	23.26	0.821	0.162	<b>23.44</b>	<b>0.822</b>	<b>0.157</b>
hku1	13.44	0.385	0.787	15.98	0.269	0.738	21.76	0.713	0.162	<b>23.82</b>	0.757	0.153	23.74	<b>0.758</b>	<b>0.149</b>
hku2	21.24	0.559	0.691	20.07	0.398	0.631	26.29	0.754	0.156	<b>29.11</b>	<b>0.798</b>	0.153	29.08	<b>0.798</b>	<b>0.148</b>
Retail_Street	18.74	0.574	0.537	17.32	0.375	0.669	21.55	0.694	0.162	24.15	0.770	0.128	<b>24.37</b>	<b>0.775</b>	<b>0.121</b>
CBD_Building_01	17.11	0.630	0.640	18.16	0.508	0.644	22.13	0.812	0.126	25.16	<b>0.851</b>	0.104	<b>25.20</b>	<b>0.851</b>	<b>0.103</b>
<b>MCD (OS1-64)</b>															
tuhh_day_02	8.72	0.158	0.893	12.65	0.295	0.766	11.15	0.478	0.350	19.99	0.621	0.312	<b>20.35</b>	<b>0.626</b>	<b>0.262</b>
tuhh_day_03	8.09	0.136	0.896	12.48	0.407	0.684	11.36	0.542	0.301	21.09	0.666	0.273	<b>21.38</b>	<b>0.672</b>	<b>0.229</b>
tuhh_day_04	11.73	0.250	0.805	13.02	0.413	0.626	13.86	0.384	0.398	<b>19.27</b>	<b>0.528</b>	0.329	<b>19.27</b>	<b>0.528</b>	<b>0.310</b>
<b>M2DGR (VLP-32C)</b>															
room_01	14.92	0.573	0.643	15.01	0.317	0.880	12.27	0.554	0.458	17.04	0.697	0.365	<b>17.45</b>	<b>0.721</b>	<b>0.282</b>
room_02	13.57	0.515	0.697	14.94	0.318	0.877	11.44	0.565	0.465	17.32	0.705	0.375	<b>17.72</b>	<b>0.725</b>	<b>0.291</b>
room_03	16.15	0.627	0.587	14.88	0.370	0.841	12.50	0.573	0.475	17.19	0.701	0.401	<b>17.38</b>	<b>0.709</b>	<b>0.334</b>

IMU bias limits accuracy. In contrast, PIN-SLAM and DBA-Fusion perform better, with PIN-SLAM in particular approaching the performance of traditional multi-sensor-based methods. Attributed to the continuous-time trajectory representation, which effectively handles LiDAR distortion and efficiently fuses high-rate IMU data, our method achieves the best localization accuracy. In non-degenerate scenarios, visual information has a relatively minor impact on localization accuracy, resulting in similar performance between *Ours-1* and *Ours-2*.

#### D. Experiment-2: Evaluation of Mapping

1) *Evaluation Protocols*: We assess the performance of photo-realistic mapping by evaluating the quality of rendered images generated from the Gaussian map. To this end, we adopt several widely used metrics, including Peak Signal-to-Noise Ratio (PSNR), Structural Similarity Index (SSIM), and Learned Perceptual Image Patch Similarity (LPIPS)[2]. Consistent with MonoGS and SplaTAM, we use AlexNet[119] as the backbone network for LPIPS evaluation. When ground-truth depth maps are available, we also evaluate geometric accuracy using Depth-L1 error computed over valid depth regions. It should be noted that we adopt *Ours-1* in the mapping evaluation and the following experiments.

Many existing methods [23, 24, 37] report rendering performance at their respective training views. However, such evaluations may be biased due to overfitting and do not reliably reflect the quality of photo-realistic mapping, particularly at novel views. To ensure a comprehensive and fair evaluation, we assess rendering quality on both in-sequence and out-of-sequence novel views, explicitly excluding training views.

In our evaluations, all compared methods are constrained to use the same training views, selected using the keyframing

strategy described in Sec. VII-A, while the remaining non-keyframes are used for evaluating in-sequence novel view rendering. To eliminate the influence of pose estimation errors on mapping performance, all methods are provided with our estimated poses for evaluation on public datasets. For our self-collected dataset where ground-truth poses are available, both our method and the baselines use ground-truth poses to avoid trajectory alignment errors, which could significantly affect the evaluation of out-of-sequence novel view rendering.

2) *In-Sequence Novel View Synthesis*: Tab. III and Tab. IV show quantitative evaluation of the rendering results of in-sequence novel views across both the public datasets and our self-collected dataset. Fig. 7 and Fig. 8 present the novel view renderings of both RGB and depth in sequence. The RGB-only method MonoGS initializes Gaussians at a preset constant depth with random noise and subsequently inserts new Gaussians based on the rendered depth statistics. In small-scale indoor scenarios, the optimization of the inserted Gaussians may gradually converge. However, it becomes much more challenging in larger scenes, where more and more Gaussians with incorrect positions accumulate, resulting in numerous floaters and poor visual quality. Incorporating LiDARs with accurate geometric priors can substantially alleviate this problem. For example, Co-SLAM leverages the LiDAR depth for ray sampling and supervision of the neural implicit map optimization, and its rendered results show relatively clear structures. It is capable of rendering beyond the LiDAR FoV based on the optimized neural representation, as shown in Fig. 7 and Fig. 8. However, the renderings of Co-SLAM appear noisy with severe artifacts, even though we specially utilize completed depth maps to guide the sampling during full-image rendering. In contrast, the LiDAR-incorporated 3DGS-based methods MM3DGS-SLAM and Gaussian-LIC exhibit better

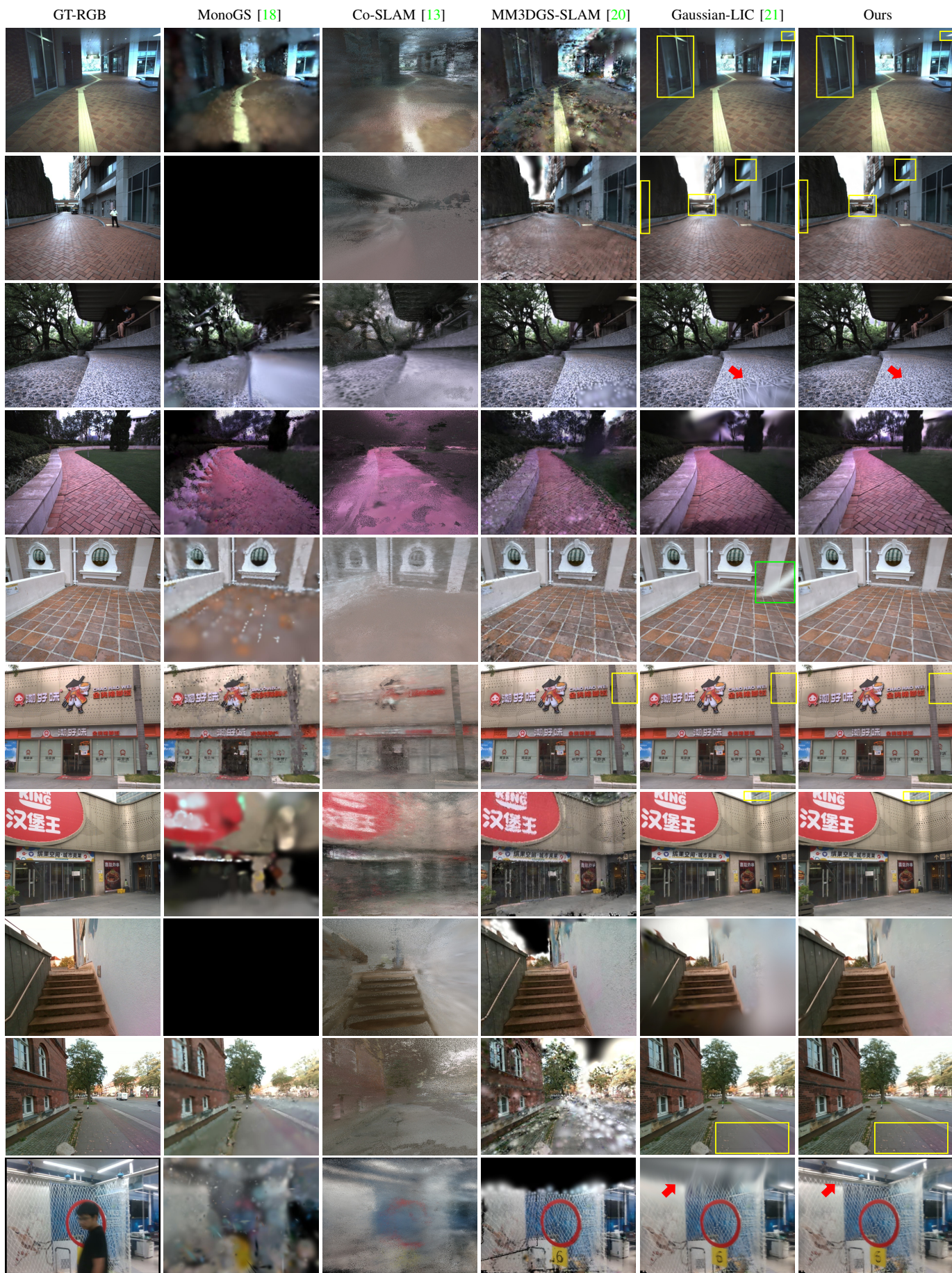


Figure 7: Qualitative results of RGB rendering (in-sequence novel view) on public datasets. Regions not observed by the LiDAR throughout the entire process are indicated by the red arrow, floaters are highlighted with green boxes, and key details are marked with yellow boxes.

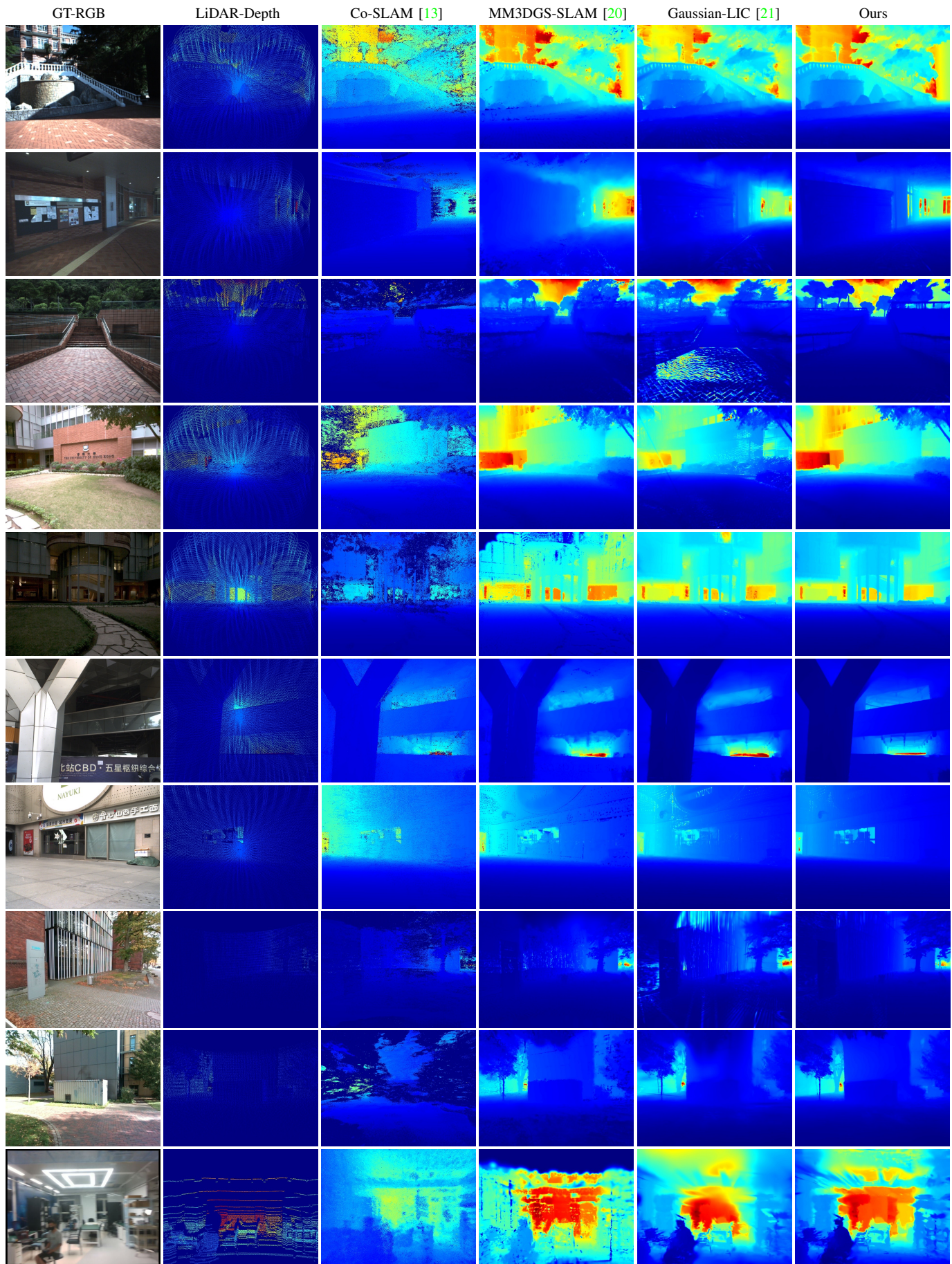


Figure 8: Qualitative results of depth rendering (in-sequence novel view) on public datasets. Sparse LiDAR depth at the viewpoints is also shown in the second column.

Table IV: Evaluation of RGB and depth rendering (in-sequence &amp; out-of-sequence novel view) on self-collected datasets. Depth-L1 (m).

LiDAR	Sequence	Method	In-Sequence Novel View				Out-of-Sequence Novel View			
			PSNR $\uparrow$	SSIM $\uparrow$	LPIPS $\downarrow$	Depth-L1 $\downarrow$	PSNR $\uparrow$	SSIM $\uparrow$	LPIPS $\downarrow$	Depth-L1 $\downarrow$
Mid-360	Liberal_Arts_Group_01	MM3DGS-SLAM [20]	22.89	0.721	0.298	0.65	21.05	0.653	0.360	0.65
		Gaussian-LIC [21]	25.12	0.759	0.297	0.92	22.08	0.670	0.350	0.81
		Ours	<b>25.35</b>	<b>0.761</b>	<b>0.278</b>	<b>0.29</b>	<b>22.10</b>	<b>0.671</b>	<b>0.332</b>	<b>0.30</b>
	Liberal_Arts_Group_02	MM3DGS-SLAM [20]	17.96	0.574	0.271	0.67	16.98	0.444	0.351	0.72
		Gaussian-LIC [21]	23.02	0.703	0.210	0.66	19.95	0.520	0.275	0.71
		Ours	<b>23.42</b>	<b>0.713</b>	<b>0.186</b>	<b>0.30</b>	<b>20.05</b>	<b>0.528</b>	<b>0.256</b>	<b>0.37</b>
	Liberal_Arts_Group_03	MM3DGS-SLAM [20]	17.74	0.493	0.385	0.96	13.87	0.347	0.478	1.22
		Gaussian-LIC [21]	22.59	0.656	0.236	0.89	<b>18.28</b>	0.458	0.351	1.25
		Ours	<b>22.79</b>	<b>0.662</b>	<b>0.222</b>	<b>0.44</b>	<b>18.28</b>	<b>0.459</b>	<b>0.345</b>	<b>0.67</b>
Medical_Building_01	MM3DGS-SLAM [20]	16.45	0.642	0.266	1.24	16.43	0.574	0.321	1.34	
	Gaussian-LIC [21]	22.77	0.737	0.199	1.28	19.40	0.632	0.268	1.64	
	Ours	<b>22.89</b>	<b>0.741</b>	<b>0.188</b>	<b>0.62</b>	<b>19.54</b>	<b>0.633</b>	<b>0.257</b>	<b>0.84</b>	
Medical_Building_02	MM3DGS-SLAM [20]	16.29	0.685	0.217	0.91	19.62	0.679	0.222	0.75	
	Gaussian-LIC [21]	<b>23.15</b>	0.758	0.177	1.53	21.33	0.685	0.216	1.35	
	Ours	23.11	<b>0.760</b>	<b>0.174</b>	<b>0.54</b>	<b>21.57</b>	<b>0.691</b>	<b>0.213</b>	<b>0.53</b>	
Avia	Lecture_Hall	MM3DGS-SLAM [20]	19.54	0.671	0.198	0.74	18.73	0.624	0.236	0.75
		Gaussian-LIC [21]	21.60	0.710	0.178	0.68	20.32	0.669	0.207	0.73
		Ours	<b>21.78</b>	<b>0.719</b>	<b>0.167</b>	<b>0.39</b>	<b>20.40</b>	<b>0.672</b>	<b>0.205</b>	<b>0.45</b>
	Robot_Center	MM3DGS-SLAM [20]	18.83	0.631	0.190	0.59	16.63	0.558	0.260	0.47
		Gaussian-LIC [21]	22.89	0.693	0.206	0.92	<b>18.81</b>	0.600	0.264	0.79
		Ours	<b>22.95</b>	<b>0.699</b>	<b>0.188</b>	<b>0.29</b>	18.80	<b>0.602</b>	<b>0.257</b>	<b>0.25</b>
	Bell_Tower_01	MM3DGS-SLAM [20]	18.13	0.600	0.300	0.67	16.40	0.592	0.299	0.74
		Gaussian-LIC [21]	25.38	0.717	0.282	0.92	<b>22.87</b>	<b>0.676</b>	0.324	0.91
		Ours	<b>25.53</b>	<b>0.720</b>	<b>0.256</b>	<b>0.27</b>	<b>22.87</b>	<b>0.676</b>	<b>0.298</b>	<b>0.35</b>
Bell_Tower_02	MM3DGS-SLAM [20]	16.49	0.661	0.278	0.87	17.01	0.620	0.320	1.14	
	Gaussian-LIC [21]	26.42	0.751	0.285	1.18	23.68	<b>0.716</b>	0.321	1.77	
	Ours	<b>26.85</b>	<b>0.756</b>	<b>0.242</b>	<b>0.29</b>	<b>24.17</b>	0.708	<b>0.276</b>	<b>0.41</b>	
Bell_Tower_03	MM3DGS-SLAM [20]	16.61	0.651	0.256	0.90	14.08	0.603	0.294	1.02	
	Gaussian-LIC [21]	27.29	0.748	0.296	1.47	25.02	0.735	0.278	1.68	
	Ours	<b>27.63</b>	<b>0.756</b>	<b>0.244</b>	<b>0.33</b>	<b>25.43</b>	<b>0.738</b>	<b>0.238</b>	<b>0.42</b>	

rendering performance. They reliably initialize Gaussians from precise LiDAR points. Nonetheless, MM3DGS-SLAM represents the scene as isotropic and view-independent Gaussians to improve running speed, but unfortunately still fails to achieve real-time performance while sacrificing the visual quality. Note that MM3DGS-SLAM uses around three times as many Gaussians as our method to model the scene. Gaussian-LIC underutilizes precise LiDAR depth and ignores to optimize the geometric quality of the Gaussian map, leading to poor-quality rendered depth. In addition, both methods struggle to accurately reconstruct areas unobserved by the LiDAR.

Our method attains the best in-sequence novel view rendering performance, both quantitatively and qualitatively. The system renders sharper RGB images with fewer artifacts at novel views, beyond only overfitting to the training views. It successfully reconstructs regions never scanned by the LiDAR, such as the ceiling beyond the reach of the VLP-32C, as demonstrated in the last row of Fig. 7. Moreover, despite relying on sparse LiDAR depth, our method is able to produce high-quality depth maps across different LiDAR modalities. It is worth noting that severe rolling shutter distortion in the images of the M2DGR dataset affects the quality of the rendered depth, as illustrated in the last row of Fig. 8.

3) *Out-of-Sequence Novel View Synthesis*: We further evaluate out-of-sequence novel view rendering on our self-collected dataset, which presents a greater challenge than in-sequence rendering. For this assessment, views are sampled

at 10 Hz along the out-of-sequence trajectory. As shown in Tab. IV, our method achieves the best results. Fig. 9 illustrates the camera trajectories and the corresponding novel view rendering results along the out-of-sequence path. Compared to our closest baseline, Gaussian-LIC, our Gaussian map is more effectively regularized and optimized, leading to sharper and higher-fidelity novel view synthesis with fewer artifacts.

### E. Experiment-3: Offline Gaussian Mapping

As a SLAM system, our method incrementally estimates poses and constructs a photo-realistic map from sequential sensor data, enabling real-time perception for robotic applications. In contrast, offline methods disregard incremental or online processing capabilities and typically perform heavy, computationally intensive optimization only after all sensor data has been collected. Existing offline Gaussian Mapping methods typically fall into two paradigms, namely per-scene optimization and generalizable feed-forward models.

1) *Per-Scene Optimization*: We first compare our method to the state-of-the-art LiDAR-based 3DGS framework, LetsGo [70], on the *Lecture\_Hall* sequence, which spans 105 seconds. To ensure a fair comparison, LetsGo is provided with the same sparse LiDAR depth maps and our estimated poses. Additionally, it uses the same set of training views as our method and is trained for 30,000 iterations. Tab. V presents the results, where we report the total time from the

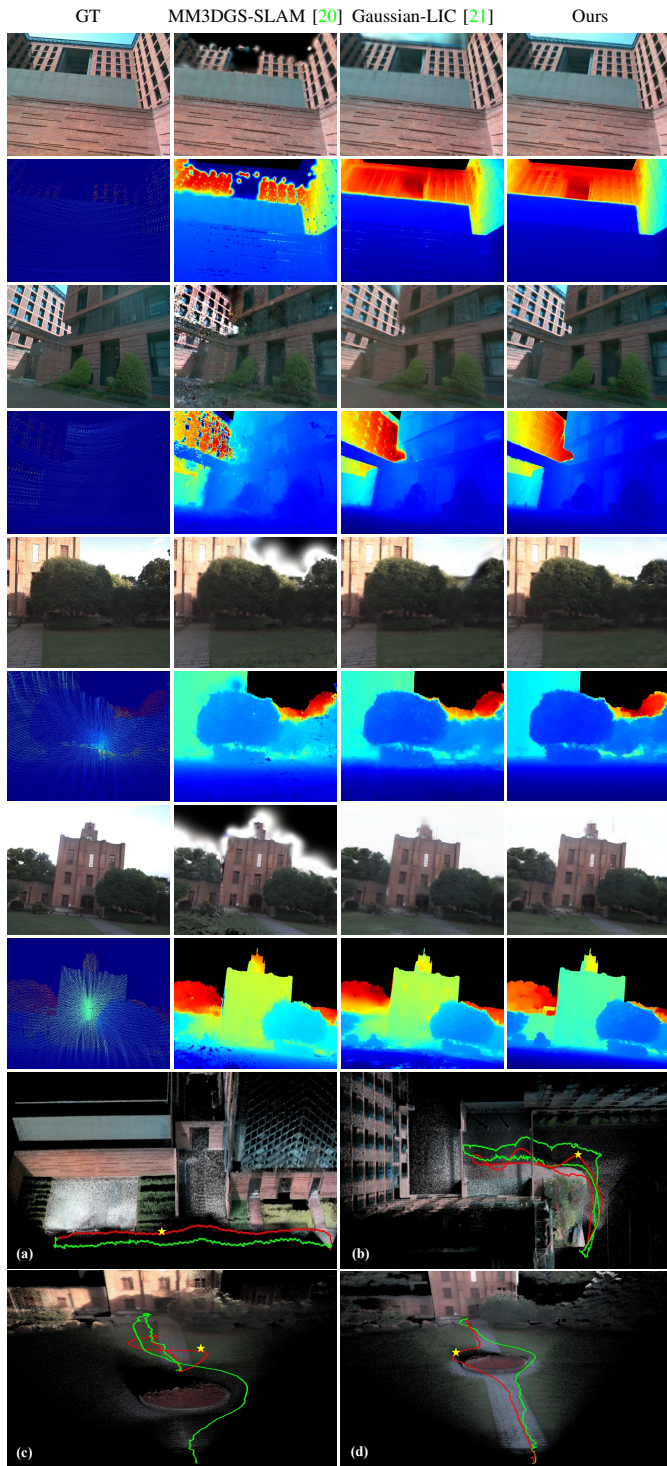


Figure 9: Qualitative results of RGB and depth rendering (out-of-sequence novel view) on our self-collected dataset. (a-d) The green path represents the trajectory for collecting training views, the red path shows the out-of-sequence trajectory for evaluation, and the yellow stars indicate the selected out-of-sequence novel views. The sky regions in rendered depth maps are masked in black.

beginning of data acquisition to the completion of reconstruction. While LetsGo performs time-consuming optimization after receiving the full dataset, our method completes the reconstruction within the duration of data acquisition and

Table V: Comparison with LiDAR-based offline Gaussian mapping method on the sequence *Lecture\_Hall* (span: 105 seconds). The total time consumption reported here is the duration of data acquisition time + reconstruction time.

	PSNR $\uparrow$	SSIM $\uparrow$	LPIPS $\downarrow$	Depth-L1 (m) $\downarrow$	Time (s) $\downarrow$
LetsGo [70]	21.81	0.708	0.170	<b>0.37</b>	105 + 347
Ours	21.78	0.719	0.167	0.39	<b>105</b>
Ours-W-Refine	<b>22.28</b>	<b>0.730</b>	<b>0.148</b>	<b>0.37</b>	105 + 24

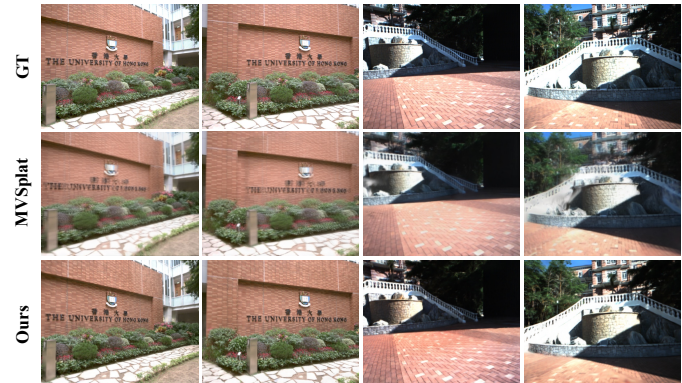


Figure 10: Comparison with the feed-forward method, MVSpLat [76]. Image renderings from both MVSpLat and ours are shown.

still achieves comparable performance. Furthermore, after an additional 10,000 iterations of refinement (requiring only 24 seconds), our method significantly outperforms LetsGo. This demonstrates that our approach not only supports real-time reconstruction but can also achieve higher accuracy when post-acquisition optimization is permitted.

2) *Feed-Forward Model*: We also compare our method with the state-of-the-art feed-forward Gaussian mapping approach, MVSpLat [76], which predicts a Gaussian map from a small set of posed images (two by default). For achieving good performance with MVSpLat, we carefully select a pair of images that provides sufficient parallax and maximal scene coverage, using poses estimated by our method. Fig. 10 shows the rendering results on the *degenerate\_seq\_00* and *hku1* sequences. While MVSpLat is capable of predicting pixel-aligned Gaussians within seconds, it often produces blurry renderings and suffers from parallax sensitivity. In contrast, our method consistently generates sharp, photo-realistic images.

### F. Runtime Analysis

We evaluate the real-time performance of our method across all datasets. Following the definition in Gaussian-LIC [21], a system is considered to be real-time capable if it completes processing within the duration of sensor data acquisition, without extensive post-processing. During runtime analysis, we evaluate our implementation using *Ours-1* as the tracking module for pose estimation. The system achieves an average pose estimation frequency of 10 Hz, while depth completion inference requires only 10–20 ms per frame. Therefore, we primarily focus on the time consumption in the mapping thread. As shown in Tab. VI, the most time-consuming components in the mapping thread are primarily the forward and backward pass of the rasterizer as well as the Adam optimizer up-

Table VI: Runtime Analysis (Time unit: s). Fwd.: forward time; Bwd.: backward time; Adam: optimizer update time; Total: total mapping time; Dur.: rosbag duration; Len.: trajectory length (m).

	Fwd.	Bwd.	Adam	Total	Dur.	Len.
<b>R3LIVE</b>						
degenerate_seq_00	9	16	9	38	87	42
degenerate_seq_01	11	15	8	38	86	61
hku_campus_seq_00	69	69	45	195	202	172
hku_campus_seq_01	154	73	48	285	304	337
hku_park_00	62	87	55	218	228	212
hku_park_01	138	112	73	340	362	354
<b>FAST-LIVO</b>						
LiDAR_Degenerate	7	12	6	29	78	38
Visual_Challenge	18	29	14	71	162	78
hku1	20	28	15	71	128	64
hku2	13	21	11	51	105	59
Retail_Street	15	26	15	64	135	66
CBD_Building_01	12	19	10	48	119	33
<b>MCD</b>						
tuhh_day_02	74	57	35	179	200	306
tuhh_day_03	70	56	34	173	200	276
tuhh_day_04	43	46	27	127	187	298
<b>M2DGR</b>						
room01	9	17	11	40	75	27
room02	8	16	10	38	89	46
room03	21	43	28	100	195	71
<b>Self-collected</b>						
Liberal_Arts_Group_01	8	9	3	24	101	42
Liberal_Arts_Group_02	23	35	16	88	225	59
Liberal_Arts_Group_03	39	50	25	132	285	102
Medical_Building_01	9	10	4	28	113	53
Medical_Building_02	10	12	4	32	120	38
Lecture_Hall	9	15	6	36	105	45
Robot_Center	18	25	13	63	136	53
Bell_Tower_01	36	30	15	90	150	67
Bell_Tower_02	13	18	9	45	103	39
Bell_Tower_03	18	19	9	52	120	48



Figure 11: Application – Video Frame Interpolation: The images in the middle are the interpolated frames at the intermediate timestamps of the left and right images.

date. Thanks to carefully designed CUDA-related acceleration strategies for these components described in Sec. VIII-B, the time for finishing mapping remains within the bag duration, showcasing the real-time capability of our method.

## XI. APPLICATIONS

### A. Video Frame Interpolation

The continuous-time trajectory enables pose querying at any valid timestamp, while the Gaussian map allows rendering from arbitrary viewpoints. Interestingly, combining these capabilities facilitates spatiotemporal interpolation, which can be applied to video interpolation. As in Fig. 11, after obtaining the continuous-time trajectory and Gaussian map from our

system, we successfully double the frame rate of the sequence *Visual\_Challenge* from 15 Hz to 30 Hz by rendering intermediate frames with poses queried at the middle time instant.

### B. Rapid 3D Mesh Extraction

Compared to previous LiDAR-Inertial-Camera 3DGS-based SLAM methods, our approach balances visual quality, geometric accuracy, and computational efficiency. In this application, we showcase how our method can be adapted for rapid meshing. We increase the depth regularization weight  $\xi$  (see (18)) to be 2, and run our system in real time within the duration of data acquisition. Subsequently, based on the reconstructed Gaussian map, we render RGB images and depth maps from all viewpoints. These rendered depth maps are fused using TSDF fusion [120] (with a voxel size of 0.05m) to reconstruct a 3D-consistent map. An accurate mesh is then extracted from the TSDF volume using the Marching Cubes algorithm [121]. Fig. 12 illustrates the resulting mesh, textured with RGB colors or colorized by surface normal directions.

## XII. CONCLUSIONS AND FUTURE WORK

In this paper, We propose a novel LiDAR-Inertial-Camera Gaussian Splatting SLAM system that jointly considers visual quality, geometric accuracy, and real-time performance. Our method enables accurate pose estimation and photo-realistic map construction in real time, supporting high-quality RGB and depth rendering. Markedly, we incorporate a zero-shot depth completion model that fuses RGB and sparse LiDAR data to generate dense depth maps, which facilitate initialization of Gaussians in large-scale scenarios. The training of the Gaussian map is efficiently supervised by our curated sparse LiDAR depth and accelerated with meticulously designed CUDA-related strategies. Meanwhile, we explore tightly fusing the visual photometric constraints derived from the Gaussian map with the LiDAR-inertial data within the continuous-time framework, effectively overcoming the LiDAR degradation. We also extend our system to support downstream tasks such as video interpolation and rapid mesh generation. Finally, we introduce a dedicated self-collected LiDAR-Inertial-Camera dataset for benchmarking photometric and geometric mapping in large-scale scenarios, with ground-truth poses and depth maps, as well as out-of-sequence trajectories. Extensive experiments shows that our system outperforms existing methods in various aspects.

Our method enhances the real-time perception capabilities of mobile robotic systems in large-scale scenarios. However, there are still several limitations, which we aim to address in future work. (1) Compactness: We currently do not impose constraints on map size, which may result in large memory usage. It is worth investigating to reduce the number of Gaussians while maintaining the map quality. (2) Geometric Accuracy: There remains a trade-off between visual quality and geometric accuracy. We aim to further improve geometric precision without sacrificing visual fidelity. (3) Applicability in Giga Scene: In extremely large-scale environments, our system may accumulate pose drift over time. We plan to introduce loop closures to mitigate this issue. (4) Integration



Figure 12: Application – 3D Mesh Extraction: Textured and normal-colored meshes generated from our reconstructed Gaussian map.

with Foundation Models: Leveraging foundation models for feed-forward Gaussian prediction, combined with generative models, presents a promising direction for improving novel view synthesis performance in out-of-sequence scenarios.

### REFERENCES

- [1] B. Mildenhall, P. P. Srinivasan, M. Tancik, J. T. Barron, R. Ramamoorthi, and R. Ng. "Nerf: Representing scenes as neural radiance fields for view synthesis". In: *Communications of the ACM* 65.1 (2021), pp. 99–106.
- [2] B. Kerbl, G. Kopanas, T. Leimkühler, and G. Drettakis. "3D Gaussian Splatting for Real-Time Radiance Field Rendering". In: *ACM Transactions on Graphics* 42.4 (2023).
- [3] F. Tosi, Y. Zhang, Z. Gong, E. Sandström, S. Mattoccia, M. R. Oswald, and M. Poggi. "How NeRFs and 3D Gaussian Splatting are Reshaping SLAM: a Survey". In: *arXiv preprint arXiv:2402.13255* (2024).
- [4] R. Jin, Y. Gao, Y. Wang, Y. Wu, H. Lu, C. Xu, and F. Gao. "Gs-planner: A gaussian-splatting-based planning framework for active high-fidelity reconstruction". In: *2024 IEEE/RSJ International Conference on Intelligent Robots and Systems (IROS)*. IEEE, 2024, pp. 11202–11209.
- [5] T. Chen, O. Shorinwa, J. Bruno, A. Swann, J. Yu, W. Zeng, K. Nagami, P. Dames, and M. Schwager. "Splat-nav: Safe real-time robot navigation in gaussian splatting maps". In: *IEEE Transactions on Robotics* (2025).
- [6] X. Lei, M. Wang, W. Zhou, and H. Li. "Gaussnav: Gaussian splatting for visual navigation". In: *IEEE Transactions on Pattern Analysis and Machine Intelligence* (2025).
- [7] W. Jiang, B. Lei, K. Ashton, and K. Daniilidis. "Ag-slam: Active gaussian splatting slam". In: (2024).
- [8] L. Chen, H. Zhan, K. Chen, X. Xu, Q. Yan, C. Cai, and Y. Xu. "ActiveG-AMER: Active GAussian Mapping through Efficient Rendering". In: *arXiv preprint arXiv:2501.06897* (2025).
- [9] H. Zhang, Y. Zou, Z. Yan, and H. Cheng. "Rapid-Mapping: LiDAR-Visual Implicit Neural Representations for Real-Time Dense Mapping". In: *IEEE Robotics and Automation Letters* (2024).
- [10] E. Sucar, S. Liu, J. Ortiz, and A. J. Davison. "iMAP: Implicit mapping and positioning in real-time". In: *Proceedings of the IEEE/CVF International Conference on Computer Vision*. 2021, pp. 6229–6238.
- [11] Z. Zhu, S. Peng, V. Larsson, W. Xu, H. Bao, Z. Cui, M. R. Oswald, and M. Pollefeys. "Nice-slam: Neural implicit scalable encoding for slam". In: *Proceedings of the IEEE/CVF Conference on Computer Vision and Pattern Recognition*. 2022, pp. 12786–12796.
- [12] X. Yang, H. Li, H. Zhai, Y. Ming, Y. Liu, and G. Zhang. "Vox-Fusion: Dense tracking and mapping with voxel-based neural implicit representation". In: *2022 IEEE International Symposium on Mixed and Augmented Reality (ISMAR)*. IEEE, 2022, pp. 499–507.
- [13] H. Wang, J. Wang, and L. Agapito. "Co-SLAM: Joint Coordinate and Sparse Parametric Encodings for Neural Real-Time SLAM". In: *Proceedings of the IEEE/CVF Conference on Computer Vision and Pattern Recognition*. 2023, pp. 13293–13302.
- [14] M. M. Johari, C. Carta, and F. Fleuret. "Eslam: Efficient dense slam system based on hybrid representation of signed distance fields". In: *Proceedings of the IEEE/CVF Conference on Computer Vision and Pattern Recognition*. 2023, pp. 17408–17419.
- [15] C. Yan, D. Qu, D. Xu, B. Zhao, Z. Wang, D. Wang, and X. Li. "Gs-slam: Dense visual slam with 3d gaussian splatting". In: *Proceedings of the IEEE/CVF Conference on Computer Vision and Pattern Recognition*. 2024, pp. 19595–19604.
- [16] N. Keetha, J. Karhade, K. M. Jatavallabhula, G. Yang, S. Scherer, D. Ramanan, and J. Luiten. "SplatTAM: Splat Track & Map 3D Gaussians for Dense RGB-D SLAM". In: *Proceedings of the IEEE/CVF Conference on Computer Vision and Pattern Recognition*. 2024, pp. 21357–21366.
- [17] V. Yugay, Y. Li, T. Gevers, and M. R. Oswald. "Gaussian-slam: Photo-realistic dense slam with gaussian splatting". In: *arXiv preprint arXiv:2312.10070* (2023).

- [18] H. Matsuki, R. Murai, P. H. Kelly, and A. J. Davison. "Gaussian splatting slam". In: *Proceedings of the IEEE/CVF Conference on Computer Vision and Pattern Recognition*. 2024, pp. 18039–18048.
- [19] H. Huang, L. Li, H. Cheng, and S.-K. Yeung. "Photo-SLAM: Real-time Simultaneous Localization and Photorealistic Mapping for Monocular Stereo and RGB-D Cameras". In: *Proceedings of the IEEE/CVF Conference on Computer Vision and Pattern Recognition*. 2024, pp. 21584–21593.
- [20] L. C. Sun, N. P. Bhatt, J. C. Liu, Z. Fan, Z. Wang, T. E. Humphreys, and U. Topcu. "Mm3dgs slam: Multi-modal 3d gaussian splatting for slam using vision, depth, and inertial measurements". In: *2024 IEEE/RSJ International Conference on Intelligent Robots and Systems (IROS)*. IEEE. 2024, pp. 10159–10166.
- [21] X. Lang, L. Li, C. Wu, C. Zhao, L. Liu, Y. Liu, J. Lv, and X. Zuo. "Gaussian-LiC: Real-Time Photo-Realistic SLAM with Gaussian Splatting and LiDAR-Inertial-Camera Fusion". In: *arXiv preprint arXiv:2404.06926* (2024).
- [22] R. Xiao, W. Liu, Y. Chen, and L. Hu. "LiV-GS: LiDAR-Vision Integration for 3D Gaussian Splatting SLAM in Outdoor Environments". In: *IEEE Robotics and Automation Letters* (2024).
- [23] H. Zhao, W. Guan, and P. Lu. "LVI-GS: Tightly-coupled LiDAR-Visual-Inertial SLAM using 3D Gaussian Splatting". In: *IEEE Transactions on Instrumentation and Measurement* (2025).
- [24] S. Hong, C. Zheng, Y. Shen, C. Li, F. Zhang, T. Qin, and S. Shen. "GS-LIVO: Real-Time LiDAR, Inertial, and Visual Multi-sensor Fused Odometry with Gaussian Mapping". In: *arXiv preprint arXiv:2501.08672* (2025).
- [25] J. Zhang and S. Singh. "Laser-visual-inertial odometry and mapping with high robustness and low drift". In: *Journal of field robotics* 35.8 (2018), pp. 1242–1264.
- [26] X. Zuo, P. Geneva, W. Lee, Y. Liu, and G. Huang. "Lic-fusion: Lidar-inertial-camera odometry". In: *2019 IEEE/RSJ International Conference on Intelligent Robots and Systems (IROS)*. IEEE. 2019, pp. 5848–5854.
- [27] X. Zuo, Y. Yang, P. Geneva, J. Lv, Y. Liu, G. Huang, and M. Pollefeys. "Lic-fusion 2.0: Lidar-inertial-camera odometry with sliding-window plane-feature tracking". In: *2020 IEEE/RSJ International Conference on Intelligent Robots and Systems (IROS)*. IEEE. 2020, pp. 5112–5119.
- [28] T. Shan, B. Englot, C. Ratti, and D. Rus. "Lvi-sam: Tightly-coupled lidar-visual-inertial odometry via smoothing and mapping". In: *2021 IEEE international conference on robotics and automation (ICRA)*. IEEE. 2021, pp. 5692–5698.
- [29] J. Lin, C. Zheng, W. Xu, and F. Zhang. "R<sup>2</sup>LIVE: A Robust, Real-Time, LiDAR-Inertial-Visual Tightly-Coupled State Estimator and Mapping". In: *IEEE Robotics and Automation Letters* 6.4 (2021), pp. 7469–7476.
- [30] J. Lin and F. Zhang. "R 3 LIVE: A Robust, Real-time, RGB-colored, LiDAR-Inertial-Visual tightly-coupled state Estimation and mapping package". In: *2022 International Conference on Robotics and Automation (ICRA)*. IEEE. 2022, pp. 10672–10678.
- [31] J. Lin and F. Zhang. "R<sup>3</sup>LIVE++: A Robust, Real-time, Radiance Reconstruction Package with a Tightly-coupled LiDAR-Inertial-Visual State Estimator". In: *IEEE Transactions on Pattern Analysis and Machine Intelligence* (2024).
- [32] C. Zheng, Q. Zhu, W. Xu, X. Liu, Q. Guo, and F. Zhang. "Fast-livo: Fast and tightly-coupled sparse-direct lidar-inertial-visual odometry". In: *2022 IEEE/RSJ International Conference on Intelligent Robots and Systems (IROS)*. IEEE. 2022, pp. 4003–4009.
- [33] C. Zheng, W. Xu, Z. Zou, T. Hua, C. Yuan, D. He, B. Zhou, Z. Liu, J. Lin, F. Zhu, et al. "Fast-livo2: Fast, direct lidar-inertial-visual odometry". In: *IEEE Transactions on Robotics* (2024).
- [34] J. Lv, X. Lang, J. Xu, M. Wang, Y. Liu, and X. Zuo. "Continuous-time fixed-lag smoothing for lidar-inertial-camera slam". In: *IEEE/ASME Transactions on Mechatronics* 28.4 (2023), pp. 2259–2270.
- [35] X. Lang, C. Chen, K. Tang, Y. Ma, J. Lv, Y. Liu, and X. Zuo. "Cocolic: continuous-time tightly-coupled lidar-inertial-camera odometry using non-uniform b-spline". In: *IEEE Robotics and Automation Letters* 8.11 (2023), pp. 7074–7081.
- [36] C. Wu, Y. Duan, X. Zhang, Y. Sheng, J. Ji, and Y. Zhang. "MM-Gaussian: 3D Gaussian-based multi-modal fusion for localization and reconstruction in unbounded scenes". In: *2024 IEEE/RSJ International Conference on Intelligent Robots and Systems (IROS)*. IEEE. 2024, pp. 12287–12293.
- [37] Y. Xie, Z. Huang, J. Wu, and J. Ma. "GS-LIVM: Real-Time Photo-Realistic LiDAR-Inertial-Visual Mapping with Gaussian Splatting". In: *arXiv preprint arXiv:2410.17084* (2024).
- [38] T. Qin, P. Li, and S. Shen. "Vins-mono: A robust and versatile monocular visual-inertial state estimator". In: *IEEE transactions on robotics* 34.4 (2018), pp. 1004–1020.
- [39] C. Campos, R. Elvira, J. J. G. Rodríguez, J. M. Montiel, and J. D. Tardós. "Orb-slam3: An accurate open-source library for visual, visual-inertial, and multimap slam". In: *IEEE transactions on robotics* 37.6 (2021), pp. 1874–1890.
- [40] R. A. Newcombe, S. J. Lovegrove, and A. J. Davison. "DTAM: Dense tracking and mapping in real-time". In: *2011 international conference on computer vision*. IEEE. 2011, pp. 2320–2327.
- [41] M. Pizzoli, C. Forster, and D. Scaramuzza. "REMODE: Probabilistic, monocular dense reconstruction in real time". In: *2014 IEEE international conference on robotics and automation (ICRA)*. IEEE. 2014, pp. 2609–2616.
- [42] J. Engel, V. Koltun, and D. Cremers. "Direct sparse odometry". In: *IEEE transactions on pattern analysis and machine intelligence* 40.3 (2017), pp. 611–625.
- [43] Z. Teed and J. Deng. "Droid-slam: Deep visual slam for monocular, stereo, and rgb-d cameras". In: *Advances in neural information processing systems* 34 (2021), pp. 16558–16569.
- [44] R. A. Newcombe, S. Izadi, O. Hilliges, D. Molyneux, D. Kim, A. J. Davison, P. Kohi, J. Shotton, S. Hodges, and A. Fitzgibbon. "Kinectfusion: Real-time dense surface mapping and tracking". In: *2011 10th IEEE international symposium on mixed and augmented reality*. Ieee. 2011, pp. 127–136.
- [45] T. Whelan, S. Leutenegger, R. F. Salas-Moreno, B. Glocker, and A. J. Davison. "ElasticFusion: Dense SLAM without a pose graph." In: *Robotics: science and systems*. Vol. 11. Rome. 2015, p. 3.
- [46] T. Schöps, T. Sattler, and M. Pollefeys. "Surfelmeshing: Online surfel-based mesh reconstruction". In: *IEEE transactions on pattern analysis and machine intelligence* 42.10 (2019), pp. 2494–2507.
- [47] S. Fridovich-Keil, A. Yu, M. Tancik, Q. Chen, B. Recht, and A. Kanazawa. "Plenoxels: Radiance fields without neural networks". In: *Proceedings of the IEEE/CVF conference on computer vision and pattern recognition*. 2022, pp. 5501–5510.
- [48] T. Müller, A. Evans, C. Schied, and A. Keller. "Instant neural graphics primitives with a multiresolution hash encoding". In: *ACM transactions on graphics (TOG)* 41.4 (2022), pp. 1–15.
- [49] L. Yariv, J. Gu, Y. Kasten, and Y. Lipman. "Volume rendering of neural implicit surfaces". In: *Advances in Neural Information Processing Systems* 34 (2021), pp. 4805–4815.
- [50] P. Wang, L. Liu, Y. Liu, C. Theobalt, T. Komura, and W. Wang. "Neus: Learning neural implicit surfaces by volume rendering for multi-view reconstruction". In: *arXiv preprint arXiv:2106.10689* (2021).
- [51] Y. Wang, Q. Han, M. Habermann, K. Daniilidis, C. Theobalt, and L. Liu. "Neus2: Fast learning of neural implicit surfaces for multi-view reconstruction". In: *Proceedings of the IEEE/CVF International Conference on Computer Vision*. 2023, pp. 3295–3306.
- [52] T. Lu, M. Yu, L. Xu, Y. Xiangli, L. Wang, D. Lin, and B. Dai. "Scaffold-gs: Structured 3d gaussians for view-adaptive rendering". In: *Proceedings of the IEEE/CVF Conference on Computer Vision and Pattern Recognition*. 2024, pp. 20654–20664.
- [53] A. Guédon and V. Lepetit. "Sugar: Surface-aligned gaussian splatting for efficient 3d mesh reconstruction and high-quality mesh rendering". In: *Proceedings of the IEEE/CVF Conference on Computer Vision and Pattern Recognition*. 2024, pp. 5354–5363.
- [54] Z. Yu, T. Sattler, and A. Geiger. "Gaussian opacity fields: Efficient adaptive surface reconstruction in unbounded scenes". In: *ACM Transactions on Graphics (TOG)* 43.6 (2024), pp. 1–13.
- [55] B. Huang, Z. Yu, A. Chen, A. Geiger, and S. Gao. "2d gaussian splatting for geometrically accurate radiance fields". In: *ACM SIGGRAPH 2024 conference papers*. 2024, pp. 1–11.
- [56] P. Dai, J. Xu, W. Xie, X. Liu, H. Wang, and W. Xu. "High-quality surface reconstruction using gaussian surfels". In: *ACM SIGGRAPH 2024 Conference Papers*. 2024, pp. 1–11.
- [57] D. Chen, H. Li, W. Ye, Y. Wang, W. Xie, S. Zhai, N. Wang, H. Liu, H. Bao, and G. Zhang. "Pgsr: Planar-based gaussian splatting for efficient and high-fidelity surface reconstruction". In: *IEEE Transactions on Visualization and Computer Graphics* (2024).
- [58] B. Zhang, C. Fang, R. Shrestha, Y. Liang, X. Long, and P. Tan. "Rade-gs: Rasterizing depth in gaussian splatting". In: *arXiv preprint arXiv:2406.01467* (2024).
- [59] H. Chen, C. Li, and G. H. Lee. "Neusg: Neural implicit surface reconstruction with 3d gaussian splatting guidance". In: *arXiv preprint arXiv:2312.00846* (2023).
- [60] M. Yu, T. Lu, L. Xu, L. Jiang, Y. Xiangli, and B. Dai. "Gsdg: 3dgs meets sdf for improved rendering and reconstruction". In: *arXiv preprint arXiv:2403.16964* (2024).
- [61] K. Rematas, A. Liu, P. P. Srinivasan, J. T. Barron, A. Tagliasacchi, T. Funkhouser, and V. Ferrari. "Urban radiance fields". In: *Proceedings of the IEEE/CVF Conference on Computer Vision and Pattern Recognition*. 2022, pp. 12932–12942.
- [62] J. Yang, B. Ivanovic, O. Litany, X. Weng, S. W. Kim, B. Li, T. Che, D. Xu, S. Fidler, M. Pavone, et al. "Emernerf: Emergent spatial-temporal scene decomposition via self-supervision". In: *arXiv preprint arXiv:2311.02077* (2023).
- [63] Y. Tao, Y. Bhalgat, L. F. T. Fu, M. Mattamala, N. Chebrolu, and M. Fallon. "SiLVR: Scalable LiDAR-visual reconstruction with neural radiance fields for robotic inspection". In: *2024 IEEE International Conference on Robotics and Automation (ICRA)*. IEEE. 2024, pp. 17983–17989.
- [64] J. Liu, C. Zheng, Y. Wan, B. Wang, Y. Cai, and F. Zhang. "Neural Surface Reconstruction and Rendering for LiDAR-Visual Systems". In: *arXiv preprint arXiv:2409.05310* (2024).
- [65] Y. Chen, C. Gu, J. Jiang, X. Zhu, and L. Zhang. "Periodic vibration gaussian: Dynamic urban scene reconstruction and real-time rendering". In: *arXiv preprint arXiv:2311.18561* (2023).
- [66] X. Zhou, Z. Lin, X. Shan, Y. Wang, D. Sun, and M.-H. Yang. "Driving-gaussian: Composite gaussian splatting for surrounding dynamic autonomous driving scenes". In: *Proceedings of the IEEE/CVF conference on computer vision and pattern recognition*. 2024, pp. 21634–21643.
- [67] Y. Yan, H. Lin, C. Zhou, W. Wang, H. Sun, K. Zhan, X. Lang, X. Zhou, and S. Peng. "Street gaussians: Modeling dynamic urban scenes with gaussian splatting". In: *European Conference on Computer Vision*. Springer. 2024, pp. 156–173.

- [68] C. Zhao, S. Sun, R. Wang, Y. Guo, J.-J. Wan, Z. Huang, X. Huang, Y. V. Chen, and L. Ren. "TCLC-GS: Tightly Coupled LiDAR-Camera Gaussian Splatting for Autonomous Driving". In: *arXiv preprint arXiv:2404.02410* (2024).
- [69] S. Hong, J. He, X. Zheng, C. Zheng, and S. Shen. "LIV-GaussMap: LiDAR-inertial-visual fusion for real-time 3D radiance field map rendering". In: *IEEE Robotics and Automation Letters* (2024).
- [70] J. Cui, J. Cao, F. Zhao, Z. He, Y. Chen, Y. Zhong, L. Xu, Y. Shi, Y. Zhang, and J. Yu. "Letsgo: Large-scale garage modeling and rendering via lidar-assisted gaussian primitives". In: *ACM Transactions on Graphics (TOG)* 43.6 (2024), pp. 1–18.
- [71] C. Jiang, R. Gao, K. Shao, Y. Wang, R. Xiong, and Y. Zhang. "Li-gs: Gaussian splatting with lidar incorporated for accurate large-scale reconstruction". In: *IEEE Robotics and Automation Letters* (2024).
- [72] J. Liu, Y. Wan, B. Wang, C. Zheng, J. Lin, and F. Zhang. "GS-SDF: LiDAR-Augmented Gaussian Splatting and Neural SDF for Geometrically Consistent Rendering and Reconstruction". In: *arXiv preprint arXiv:2503.10170* (2025).
- [73] A. Yu, V. Ye, M. Tancik, and A. Kanazawa. "pixelnerf: Neural radiance fields from one or few images". In: *Proceedings of the IEEE/CVF conference on computer vision and pattern recognition*. 2021, pp. 4578–4587.
- [74] A. Chen, Z. Xu, F. Zhao, X. Zhang, F. Xiang, J. Yu, and H. Su. "Mvsnerf: Fast generalizable radiance field reconstruction from multi-view stereo". In: *Proceedings of the IEEE/CVF international conference on computer vision*. 2021, pp. 14124–14133.
- [75] D. Charatan, S. L. Li, A. Tagliasacchi, and V. Sitzmann. "pixelsplat: 3d gaussian splats from image pairs for scalable generalizable 3d reconstruction". In: *Proceedings of the IEEE/CVF conference on computer vision and pattern recognition*. 2024, pp. 19457–19467.
- [76] Y. Chen, H. Xu, C. Zheng, B. Zhuang, M. Pollefeys, A. Geiger, T.-J. Cham, and J. Cai. "Mvsplat: Efficient 3d gaussian splatting from sparse multi-view images". In: *European Conference on Computer Vision*. Springer, 2024, pp. 370–386.
- [77] E. Sandström, Y. Li, L. Van Gool, and M. R. Oswald. "Point-slam: Dense neural point cloud-based slam". In: *Proceedings of the IEEE/CVF International Conference on Computer Vision*. 2023, pp. 18433–18444.
- [78] C. Jiang, H. Zhang, P. Liu, Z. Yu, H. Cheng, B. Zhou, and S. Shen. "H<sub>2</sub>-mapping: Real-time dense mapping using hierarchical hybrid representation". In: *IEEE Robotics and Automation Letters* 8.10 (2023), pp. 6787–6794.
- [79] Z. Peng, T. Shao, Y. Liu, J. Zhou, Y. Yang, J. Wang, and K. Zhou. "Rtg-slam: Real-time 3d reconstruction at scale using gaussian splatting". In: *ACM SIGGRAPH 2024 Conference Papers*. 2024, pp. 1–11.
- [80] J. Wei and S. Leutenegger. "Gsfusion: Online rgb-d mapping where gaussian splatting meets tsdf fusion". In: *IEEE Robotics and Automation Letters* (2024).
- [81] Z. Zhu, S. Peng, V. Larsson, Z. Cui, M. R. Oswald, A. Geiger, and M. Pollefeys. "Nicer-slam: Neural implicit scene encoding for rgb slam". In: *2024 International Conference on 3D Vision (3DV)*. IEEE, 2024, pp. 42–52.
- [82] C.-M. Chung, Y.-C. Tseng, Y.-C. Hsu, X.-Q. Shi, Y.-H. Hua, J.-F. Yeh, W.-C. Chen, Y.-T. Chen, and W. H. Hsu. "Orbeez-slam: A real-time monocular visual slam with orb features and nerf-realized mapping". In: *2023 IEEE International Conference on Robotics and Automation (ICRA)*. IEEE, 2023, pp. 9400–9406.
- [83] A. Rosinol, J. J. Leonard, and L. Carlone. "Nerf-slam: Real-time dense monocular slam with neural radiance fields". In: *2023 IEEE/RSJ International Conference on Intelligent Robots and Systems (IROS)*. IEEE, 2023, pp. 3437–3444.
- [84] F. A. Sarikamis and A. A. Alatan. "Ig-slam: Instant gaussian slam". In: *arXiv preprint arXiv:2408.01126* (2024).
- [85] J. Naumann, B. Xu, S. Leutenegger, and X. Zuo. "NeRF-VO: Real-time sparse visual odometry with neural radiance fields". In: *IEEE Robotics and Automation Letters* (2024).
- [86] P. Zhu, Y. Zhuang, B. Chen, L. Li, C. Wu, and Z. Liu. "Mgs-slam: Monocular sparse tracking and gaussian mapping with depth smooth regularization". In: *IEEE Robotics and Automation Letters* (2024).
- [87] Z. Teed, L. Lipson, and J. Deng. "Deep patch visual odometry". In: *Advances in Neural Information Processing Systems* 36 (2023), pp. 39033–39051.
- [88] X. Zhong, Y. Pan, J. Behley, and C. Stachniss. "Shine-mapping: Large-scale 3d mapping using sparse hierarchical implicit neural representations". In: *2023 IEEE International Conference on Robotics and Automation (ICRA)*. IEEE, 2023, pp. 8371–8377.
- [89] X. Yu, Y. Liu, S. Mao, S. Zhou, R. Xiong, Y. Liao, and Y. Wang. "Nf-atlas: Multi-volume neural feature fields for large scale lidar mapping". In: *IEEE Robotics and Automation Letters* 8.9 (2023), pp. 5870–5877.
- [90] S. Song, J. Zhao, K. Huang, J. Lin, C. Ye, and T. Feng. "N<sup>3</sup>-Mapping: Normal Guided Neural Non-Projective Signed Distance Fields for Large-scale 3D Mapping". In: *IEEE Robotics and Automation Letters* (2024).
- [91] K. Wu, K. Zhang, Z. Zhang, M. Tie, S. Yuan, J. Zhao, Z. Gan, and W. Ding. "HGS-mapping: Online dense mapping using hybrid Gaussian representation in urban scenes". In: *IEEE Robotics and Automation Letters* (2024).
- [92] J. Deng, Q. Wu, X. Chen, S. Xia, Z. Sun, G. Liu, W. Yu, and L. Pei. "Nerf-loam: Neural implicit representation for large-scale incremental lidar odometry and mapping". In: *Proceedings of the IEEE/CVF International Conference on Computer Vision*. 2023, pp. 8218–8227.
- [93] S. Isaacson, P.-C. Kung, M. Ramanagopal, R. Vasudevan, and K. A. Skinner. "Loner: Lidar-only neural representations for real-time slam". In: *IEEE Robotics and Automation Letters* 8.12 (2023), pp. 8042–8049.
- [94] Y. Pan, X. Zhong, L. Wiesmann, T. Posewsky, J. Behley, and C. Stachniss. "PIN-SLAM: LiDAR SLAM using a point-based implicit neural representation for achieving global map consistency". In: *IEEE Transactions on Robotics* (2024).
- [95] E. Giacomini, L. Di Giammarino, L. De Reboti, G. Grisetti, and M. R. Oswald. "Splat-LOAM: Gaussian Splatting LiDAR Odometry and Mapping". In: *arXiv preprint arXiv:2503.17491* (2025).
- [96] Y. Pan, X. Zhong, L. Jin, L. Wiesmann, M. Popović, J. Behley, and C. Stachniss. "PINGS: Gaussian Splatting Meets Distance Fields within a Point-Based Implicit Neural Map". In: *arXiv preprint arXiv:2502.05752* (2025).
- [97] X. Lang, J. Lv, J. Huang, Y. Ma, Y. Liu, and X. Zuo. "Ctrl-VIO: Continuous-time visual-inertial odometry for rolling shutter cameras". In: *IEEE Robotics and Automation Letters* 7.4 (2022), pp. 11537–11544.
- [98] P. Geneva, K. Eickenhoff, W. Lee, Y. Yang, and G. Huang. "Openvins: A research platform for visual-inertial estimation". In: *2020 IEEE International Conference on Robotics and Automation (ICRA)*. IEEE, 2020, pp. 4666–4672.
- [99] W. Xu, Y. Cai, D. He, J. Lin, and F. Zhang. "Fast-lid2: Fast direct lidar-inertial odometry". In: *IEEE Transactions on Robotics* 38.4 (2022), pp. 2053–2073.
- [100] B. D. Lucas and T. Kanade. "An iterative image registration technique with an application to stereo vision". In: *IJCAI'81: 7th international joint conference on Artificial intelligence*. Vol. 2. 1981, pp. 674–679.
- [101] S. Agarwal, K. Mierle, and Others. *Ceres Solver*. <http://ceres-solver.org>.
- [102] L. Yang, B. Kang, Z. Huang, Z. Zhao, X. Xu, J. Feng, and H. Zhao. "Depth anything v2". In: *Advances in Neural Information Processing Systems* 37 (2024), pp. 21875–21911.
- [103] R. Wang, S. Xu, C. Dai, J. Xiang, Y. Deng, X. Tong, and J. Yang. "Moge: Unlocking accurate monocular geometry estimation for open-domain images with optimal training supervision". In: *arXiv preprint arXiv:2410.19115* (2024).
- [104] M. Hu, W. Yin, C. Zhang, Z. Cai, X. Long, H. Chen, K. Wang, G. Yu, C. Shen, and S. Shen. "Metric3d v2: A versatile monocular geometric foundation model for zero-shot metric depth and surface normal estimation". In: *IEEE Transactions on Pattern Analysis and Machine Intelligence* (2024).
- [105] A. Bochkovskii, A. Delaunoy, H. Germain, M. Santos, Y. Zhou, S. R. Richter, and V. Koltun. "Depth pro: Sharp monocular metric depth in less than a second". In: *arXiv preprint arXiv:2410.02073* (2024).
- [106] C. Cao, X. Ren, and Y. Fu. "MVSFormer: Multi-view stereo by learning robust image features and temperature-based depth". In: *arXiv preprint arXiv:2208.02541* (2022).
- [107] H. Xu, J. Zhang, J. Cai, H. Rezatofighi, F. Yu, D. Tao, and A. Geiger. "Unifying flow, stereo and depth estimation". In: *IEEE Transactions on Pattern Analysis and Machine Intelligence* 45.11 (2023), pp. 13941–13958.
- [108] Z. Liu, K. L. Cheng, Q. Wang, S. Wang, H. Ouyang, B. Tan, K. Zhu, Y. Shen, Q. Chen, and P. Luo. "DepthLab: From Partial to Complete". In: *arXiv preprint arXiv:2412.18153* (2024).
- [109] H. Lin, S. Peng, J. Chen, S. Peng, J. Sun, M. Liu, H. Bao, J. Feng, X. Zhou, and B. Kang. "Prompting Depth Anything for 4K Resolution Accurate Metric Depth Estimation". In: *arXiv preprint arXiv:2412.14015* (2024).
- [110] H. Wang, M. Yang, X. Zheng, and G. Hua. "Scale Propagation Network for Generalizable Depth Completion". In: *IEEE Transactions on Pattern Analysis and Machine Intelligence* (2024).
- [111] Z. Yan, W. F. Low, Y. Chen, and G. H. Lee. "Multi-scale 3d gaussian splatting for anti-aliased rendering". In: *Proceedings of the IEEE/CVF Conference on Computer Vision and Pattern Recognition*. 2024, pp. 20923–20931.
- [112] L. Radl, M. Steiner, M. Parger, A. Weinrauch, B. Kerbl, and M. Steinberger. "Stopthepop: Sorted gaussian splatting for view-consistent real-time rendering". In: *ACM Transactions on Graphics (TOG)* 43.4 (2024), pp. 1–17.
- [113] S. S. Mallick, R. Goel, B. Kerbl, M. Steinberger, F. V. Carrasco, and F. De La Torre. "Taming 3dgs: High-quality radiance fields with limited resources". In: *SIGGRAPH Asia 2024 Conference Papers*. 2024, pp. 1–11.
- [114] T.-M. Nguyen, S. Yuan, T. H. Nguyen, P. Yin, H. Cao, L. Xie, M. Wozniak, P. Jensfelt, M. Thiel, J. Ziegenbein, et al. "Mcd: Diverse large-scale multi-campus dataset for robot perception". In: *Proceedings of the IEEE/CVF Conference on Computer Vision and Pattern Recognition*. 2024, pp. 22304–22313.
- [115] J. Yin, A. Li, T. Li, W. Yu, and D. Zou. "M2dgr: A multi-sensor and multi-scenario slam dataset for ground robots". In: *IEEE Robotics and Automation Letters* 7.2 (2021), pp. 2266–2273.
- [116] P. Furgale, J. Rehder, and R. Siegwart. "Unified temporal and spatial calibration for multi-sensor systems". In: *2013 IEEE/RSJ International Conference on Intelligent Robots and Systems*. IEEE, 2013, pp. 1280–1286.
- [117] J. Lv, K. Hu, J. Xu, Y. Liu, X. Ma, and X. Zuo. "CLINS: Continuous-time trajectory estimation for LiDAR-inertial system". In: *2021 IEEE/RSJ International Conference on Intelligent Robots and Systems (IROS)*. IEEE, 2021, pp. 6657–6663.
- [118] Y. Zhou, X. Li, S. Li, X. Wang, S. Feng, and Y. Tan. "DBA-fusion: tightly integrating deep dense visual bundle adjustment with multiple sensors for large-scale localization and mapping". In: *IEEE Robotics and Automation Letters* (2024).
- [119] A. Krizhevsky, I. Sutskever, and G. E. Hinton. "Imagenet classification with deep convolutional neural networks". In: *Advances in neural information processing systems* 25 (2012).
- [120] B. Curless and M. Levoy. "A volumetric method for building complex models from range images". In: *Proceedings of the 23rd annual conference on Computer graphics and interactive techniques*. 1996, pp. 303–312.
- [121] W. E. Lorensen and H. E. Cline. "Marching cubes: A high resolution 3D surface construction algorithm". In: *Seminal graphics: pioneering efforts that shaped the field*. 1998, pp. 347–353.